



Universiteit Gent
Faculteit Wetenschappen
Vakgroep Fysica en Sterrenkunde

² No title yet

³ No sub-title neither, obviously...

⁴ Alexis Fagot

5



Thesis to obtain the degree of
Doctor of Philosophy in Physics
Academic years 2012-2017





Universiteit Gent
Faculteit Wetenschappen
Vakgroep Fysica en Sterrenkunde

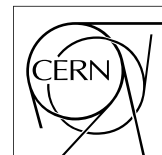
Promotoren: Dr. Michael Tytgat
Prof. Dr. Dirk Ryckbosch

Universiteit Gent
Faculteit Wetenschappen
Vakgroep Fysica en Sterrenkunde
Proeftuinstraat 86, B-9000 Gent, België
Tel.: +32 9 264.65.28
Fax.: +32 9 264.66.97

17



Thesis to obtain the degree of
Doctor of Philosophy in Physics
Academic years 2012-2017



Acknowledgements

¹⁹ Ici on remerciera tous les gens que j'ai pu croiser durant cette aventure et qui m'ont permis de passer
²⁰ un bon moment

²¹ *Gent, ici la super date de la mort qui tue de la fin d'écriture*
²² *Alexis Fagot*

Table of Contents

23

24	Acknowledgements	i
25	Nederlandse samenvatting	xv
26	English summary	xvii
27	1 Introduction	1-1
28	1.1 A story of High Energy Physics	1-1
29	1.2 Organisation of this study	1-1
30	2 Investigating the TeV scale	2-1
31	2.1 The Standard Model of Particle Physics	2-1
32	2.2 The Large Hadron Collider and the Compact Muon Solenoid	2-1
33	2.3 Muon Phase-II Upgrade	2-1
34	3 Amplification processes in gaseous detectors	3-1
35	3.1 Signal formation	3-1
36	3.2 Gas transport parameters	3-1
37	4 Resistive Plate Chambers	4-1
38	4.1 Principle	4-1
39	4.2 Rate capability of Resistive Plate Chambers	4-1
40	4.3 High time resolution	4-1
41	4.4 Resistive Plate Chambers at CMS	4-1
42	4.4.1 Overview	4-1
43	4.4.2 The present RPC system	4-2
44	4.4.3 Pulse processing of CMS RPCs	4-3
45	5 Longevity studies and Consolidation of the present CMS RPC subsystem	5-1
46	5.1 Testing detectors under extreme conditions	5-1
47	5.1.1 The Gamma Irradiation Facilities	5-3
48	5.1.1.1 GIF	5-3
49	5.1.1.2 GIF++	5-5
50	5.2 Preliminary tests at GIF	5-7
51	5.2.1 Resistive Plate Chamber test setup	5-7
52	5.2.2 Data Acquisition	5-9
53	5.2.3 Geometrical acceptance of the setup layout to cosmic muons	5-9
54	5.2.3.1 Description of the simulation layout	5-10
55	5.2.3.2 Simulation procedure	5-12
56	5.2.3.3 Results	5-13
57	5.2.4 Photon flux at GIF	5-13

58	5.2.4.1	Expectations from simulations	5-13
59	5.2.4.2	Dose measurements	5-18
60	5.2.5	Results and discussions	5-19
61	5.3	Longevity tests at GIF++	5-20
62	5.3.1	Description of the Data Acquisition	5-23
63	5.3.2	RPC current, environmental and operation parameter monitoring	5-24
64	5.3.3	Measurement procedure	5-25
65	5.3.4	Longevity studies results	5-25
66	6	Investigation on high rate RPCs	6-1
67	6.1	Rate limitations and ageing of RPCs	6-1
68	6.1.1	Low resistivity electrodes	6-1
69	6.1.2	Low noise front-end electronics	6-1
70	6.2	Construction of prototypes	6-1
71	6.3	Results and discussions	6-1
72	7	Conclusions and outlooks	7-1
73	7.1	Conclusions	7-1
74	7.2	Outlooks	7-1
75	A	A data acquisition software for CAEN VME TDCs	A-1
76	A.1	GIF++ DAQ file tree	A-1
77	A.2	Usage of the DAQ	A-2
78	A.3	Description of the readout setup	A-3
79	A.4	Data read-out	A-3
80	A.4.1	V1190A TDCs	A-4
81	A.4.2	DataReader	A-6
82	A.5	Communications	A-10
83	A.5.1	V1718 USB Bridge	A-10
84	A.5.2	Configuration file	A-11
85	A.5.3	WebDCS/DAQ intercommunication	A-14
86	A.5.4	Example of inter-process communication cycle	A-14
87	A.6	Software export	A-16
88	B	Details on the offline analysis package	B-1
89	B.1	GIF++ Offline Analysis file tree	B-1
90	B.2	Usage of the Offline Analysis	B-2
91	C	Structure of the hybrid simulation software	C-1
92	C.1	Introduction	C-1

List of Figures

93

94	2.1	Absorbed dose in the CMS cavern after an integrated luminosity of 3000 fb. R is the transverse distance from the beamline and Z is the distance along the beamline from the Interaction Point at Z=0.	2-2
95			
96			
97	2.2	A quadrant of the muon system, showing DTs (yellow), RPCs (light blue), and CSCs (green). The locations of new forward muon detectors for Phase-II are contained within the dashed box and indicated in red for GEM stations (ME0, GE1/1, and GE2/1) and dark blue for improved RPC (iRPC) stations (RE3/1 and RE4/1).	2-2
98			
99			
100			
101	2.3	RMS of the multiple scattering displacement as a function of muon p_T for the proposed forward muon stations. All of the electromagnetic processes such as bremsstrahlung and magnetic field effect are included in the simulation.	2-3
102			
103			
104	4.1	Signals from the RPC strips are shaped by the FEE described on Figure 4.1a. Output LVDS signals are then read-out by a TDC module connected to a computer or converted into NIM and sent to scalers. Figure 4.1b describes how these converted signals are put in coincidence with the trigger.	4-3
105			
106			
107			
108	4.2	Description of the principle of a CFD. A comparison of threshold triggering (left) and constant fraction triggering (right) is shown in Figure 4.2a. Constant fraction triggering is obtained thanks to zero-crossing technique as explained in Figure 4.2b. The signal arriving at the input of the CFD is split into three components. A first one is delayed and connected to the inverting input of a first comparator. A second component is connected to the noninverting input of this first comparator. A third component is connected to the noninverting input of another comparator along with a threshold value connected to the inverting input. Finally, the output of both comparators is fed through an AND gate.	4-4
109			
110			
111			
112			
113			
114			
115			
116			
117	5.1	(5.1a) Extrapolation from 2016 data of single hit rate per unit area in the barrel region. (5.1b) Extrapolation from 2016 data of single hit rate per unit area in the endcap region.	5-2
118			
119			
120	5.2	Background Fluka simulation compared to 2016 Data at $L = 10^{34} cm^{-2}.s^{-1}$ in the fourth endcap disk region. A mismatch in between simulation and data can be observed. [To be understood.]	5-3
121			
122			
123	5.3	Layout of the test beam zone called X5c GIF at CERN. Photons from the radioactive source produce a sustained high rate of random hits over the whole area. The zone is surrounded by 8 m high and 80 cm thick concrete walls. Access is possible through three entry points. Two access doors for personnel and one large gate for material. A crane allows installation of heavy equipment in the area.	5-4
124			
125			
126			
127			
128	5.4	^{137}Cs decays by β^- emission to the ground state of ^{137}Ba (BR = 5.64%) and via the 662 keV isomeric level of ^{137}Ba (BR = 94.36%) whose half-life is 2.55 min.	5-5
129			

130	5.5	Floor plan of the GIF++ facility. When the facility downstream of the GIF++ takes electron beam, a beam pipe is installed along the beam line (z-axis). The irradiator can be displaced laterally (its center moves from $x = 0.65$ m to 2.15 m), to increase the distance to the beam pipe.	5-5
131			
132	5.6	Simulated unattenuated current of photons in the xz plane (Figure 5.6a) and yz plane (Figure 5.6b) through the source at $x = 0.65$ m and $y = 0$ m. With angular correction filters, the current of 662 keV photons is made uniform in xy planes.	5-6
133			
134	5.7	Description of the RPC setup. Dimensions are given in mm. A tent containing RPCs is placed at 1720 mm from the source container. The source is situated in the center of the container. RE-4-2-BARC-161 chamber is 160 mm inside the tent. This way, the distance between the source and the chambers plan is 2060 mm. Figure 5.7a provides a side view of the setup in the xz plane while Figure 5.7b shows a top view in the yz plane.	5-7
135			
136	5.8	RE-4-2-BARC-161 chamber is inside the tent as described in Figure 5.7. In the top right, the two scintillators used as trigger can be seen. This trigger system has an inclination of 10° relative to horizontal and is placed above half-partition B2 of the RPCs. PMT electronics are shielded thanks to lead blocks placed in order to protect them without stopping photons from going through the scintillators and the chamber.	5-8
137			
138	5.9	Hit distributions over all 3 partitions of RE-4-2-BARC-161 chamber is showed on these plots. Top, middle and bottom figures respectively correspond to partitions A, B, and C. These plots show that some events still occur in other half-partitions than B2, which corresponds to strips 49 to 64, in front of which the trigger is placed, contributing to the inefficiency of detection of cosmic muons. In the case of partitions A and C, the very low amount of data can be interpreted as noise. On the other hand, it is clear that a little portion of muons reach the half-partition B1, corresponding to strips 33 to 48.	5-9
139			
140	5.10	Results are derived from data taken on half-partition B2 only. On the 18 th of June 2014, data has been taken on chamber RE-2-BARC-161 at building 904 (Prevessin Site) with cosmic muons providing us a reference efficiency plateau of $(97.54 \pm 0.15)\%$ represented by a black curve. A similar measurement has been done at GIF on the 21 st of July with the same chamber giving a plateau of $(78.52 \pm 0.94)\%$ represented by a red curve.	5-10
141			
142	5.11	Representation of the layout used for the simulations of the test setup. The RPC is represented as a yellow trapezoid while the two scintillators as blue cuboids looking at the sky. A green plane corresponds to the muon generation plane within the simulation. Figure 5.7a shows a global view of the simulated setup. Figure 5.7b shows a zommed view that allows to see the 2 scintillators as well as the full RPC plane.	5-11
143			
144	5.12	γ flux $F(D)$ is plot using values from table 5.1. As expected, the plot shows similar attenuation behaviours with increasing distance for each absorption factors.	5-14
145			
146	5.13	Figure 5.13a shows the linear approximation fit done via formulae 5.7 on data from table 5.2. Figure 5.13b shows a comparison of this model with the simulated flux using a and b given in figure 5.13a in formulae 5.4 and the reference value $D_0 = 50\text{cm}$ and the associated flux for each absorption factor F_0^{ABS} from table 5.1	5-16
147			
148	5.14	Dose measurements has been done in a plane corresponding to the tents front side. This plan is 1900 mm away from the source. As explained in the first chapter, a lens-shaped lead filter provides a uniform photon flux in the vertical plan orthogonal to the beam direction. If the second line of measured fluxes is not taken into account because of lower values due to experimental equipments in the way between the source and the tent, the uniformity of the flux is well showed by the results.	5-18
149			
150			
151			
152			
153			
154			
155			
156			
157			
158			
159			
160			
161			
162			
163			
164			
165			
166			
167			
168			
169			
170			
171			
172			
173			
174			
175			
176			
177			
178			

179	5.15	5-19
180	5.16 Evolution of the maximum efficiency for RE2 (5.16a) and RE4 (5.16b) chambers with increasing extrapolated γ rate per unit area at working point. Both irradiated (blue) and non irradiated (red) chambers are shown.	5-21
181		
182		
183	5.17 Evolution of the working point for RE2 (5.17a) and RE4 (5.17b) with increasing extrapolated γ rate per unit area at working point. Both irradiated (blue) and non irradiated (red) chambers are shown.	5-21
184		
185		
186	5.18 Evolution of the maximum efficiency at HL-LHC conditions, i.e. a background hit rate per unit area of 300 Hz/cm ² , with increasing integrated charge for RE2 (5.18a) and RE4 (5.18b) detectors. Both irradiated (blue) and non irradiated (red) chambers are shown. The integrated charge for non irradiated detectors is recorded during test beam periods and stays small with respect to the charge accumulated in irradiated chambers.	5-22
187		
188		
189		
190		
191		
192	5.19 Comparison of the efficiency sigmoid before (triangles) and after (circles) irradiation for RE2 (5.19a) and RE4 (5.19b) detectors. Both irradiated (blue) and non irradiated (red) chambers are shown.	5-22
193		
194		
195	5.20 Evolution of the Bakelite resistivity for RE2 (5.20a) and RE4 (5.20b) detectors. Both irradiated (blue) and non irradiated (red) chambers are shown.	5-23
196		
197	5.21 Evolution of the noise rate per unit area for the irradiated chamber RE2-2-BARC-9 only.	5-23
198		
199	A.1 (A.1a) View of the front panel of a V1190A TDC module [10]. (A.1b) View of the front panel of a V1718 Bridge module [11]. (A.1c) View of the front panel of a 6U 6021 VME crate [12].	A-3
200		
201		
202	A.2 Module V1190A <i>Trigger Matching Mode</i> timing diagram [10].	A-4
203		
204	A.3 Structure of the ROOT output file generated by the DAQ. The 5 branches (<code>EventNumber</code> , <code>number_of_hits</code> , <code>Quality_flag</code> , <code>TDC_channel</code> and <code>TDC_TimeStamp</code>) are visible on the left panel of the ROOT browser. On the right panel is visible the histogram cor- responding to the variable <code>nHits</code> . In this specific example, there were approximately 50k events recorded to measure the gamma irradiation rate on the detectors. Each event is stored as a single entry in the <code>TTree</code>	A-10
205		
206		
207		
208		
209	A.4 WebDCS DAQ scan page. On this page, shifters need to choose the type of scan (Rate, Efficiency or Noise Reference scan), the gamma source configuration at the moment of data taking, the beam configuration, and the trigger mode. These in- formation will be stored in the DAQ ROOT output. Are also given the minimal measurement time and waiting time after ramping up of the detectors is over before starting the data acquisition. Then, the list of HV points to scan and the number of triggers for each run of the scan are given in the table underneath.	A-12
210		
211		
212		
213		
214		
215		

List of Tables

216

217	5.1	Total photon flux ($E\gamma \leq 662$ keV) with statistical error predicted considering a	
218		^{137}Cs activity of 740 GBq at different values of the distance D to the source along	
219		the x-axis of irradiation field [6].	5-13
220	5.2	Correction factor c is computed thanks to formulae 5.5 taking as reference $D_0 =$	
221		50 cm and the associated flux F_0^{ABS} for each absorption factor available in table 5.1.	5-15
222	5.3	The data at D_0 in 1997 is taken from [6]. In a second step, using Equations 5.8	
223		and 5.9, the flux at D can be estimated in 1997. Then, taking into account the	
224		attenuation of the source activity, the flux at D can be estimated at the time of the	
225		tests in GIF in 2014. Finally, assuming a sensitivity of the RPC to γ $s = 2 \cdot 10^{-3}$,	
226		an estimation of the hit rate per unit area is obtained.	5-17
227	A.1	Inter-process communication cycles in between the webDCS and the DAQ through	
228		file string signals.	A-15

229

List of Acronyms

230

List of Acronyms

231

232

A

233

234

235 AFL Almost Full Level

236

237

B

238

239

240 BARC Bhabha Atomic Research Centre
241 BLT Block Transfer
242 BR Branching Ratio

243

244

C

245

246

247 CAEN Costruzioni Apparecchiature Elettroniche Nucleari S.p.A.
248 CERN European Organization for Nuclear Research
249 CFD Constant Fraction Discriminator
250 CMS Compact Muon Solenoid
251 CSC Cathode Strip Chamber

252

253

D

254

255

256 DAQ Data Acquisition
257 DCS Detector Control Software
258 DQM Data Quality Monitoring
259 DT Drift Tube

260

261

F

262

263

264	FEE	Front-End Electronics
265	FEB	Front-End Board
266		
267	G	
269		
270	GE-/-	Find a good description
271	GE1/1	Find a good description
272	GE2/1	Find a good description
273	GEANT	GEometry ANd Tracking - a series of software toolkit platforms developed by CERN
274		
275	GEM	Gas Electron Multiplier
276	GIF	Gamma Irradiation Facility
277	GIF++	new Gamma Irradiation Facility
278		
279	H	
280		
281		
282	HL-LHC	High Luminosity LHC
283	HV	High Voltage
284		
285	I	
286		
287		
288	iRPC	improved RPC
289	IRQ	Interrupt Request
290		
291	L	
292		
293		
294	LHC	Large Hadron Collider
295	LS1	First Long Shutdown
296	LS3	Third Long Shutdown
297	LV	Low Voltage
298	LVDS	Low-Voltage Differential Signaling
299		
300	M	
301		
302		
303	MC	Monte Carlo
304	MCNP	Monte Carlo N-Particle
305	ME-/-	Find good description
306	ME0	Find good description

307		
308	N	
309		
310		
311	NIM	Nuclear Instrumentation Module logic signals
312		
313	P	
314		
315		
316	PMT	PhotoMultiplier Tube
317		
318	R	
319		
320		
321	RE-/-	Find a good description
322	RE2/2	Find a good description
323	RE3/1	Find a good description
324	RE3/2	Find a good description
325	RE4/1	Find a good description
326	RE4/2	Find a good description
327	RE4/3	Find a good description
328	RMS	Root Mean Square
329	ROOT	a framework for data processing born at CERN
330	RPC	Resistive Plate Chamber
331		
332	S	
333		
334		
335	SPS	Super Proton Synchrotron
336		
337	T	
338		
339		
340	TDC	Time-to-Digital Converter
341		
342	W	
343		
344		
345	webDCS	Web Detector Control System

347

Nederlandse samenvatting –Summary in Dutch–

349 Le resume en Neerlandais (j'aurais peut-être de apprendre la langue juste pour ca...).

348

English summary

³⁵¹ Le meme résume mais en Anglais (on commencera par la hein!).

1

Introduction

352

353

³⁵⁴ **1.1 A story of High Energy Physics**

³⁵⁵ **1.2 Organisation of this study**

2

356

Investigating the TeV scale

358 2.1 The Standard Model of Particle Physics

359 2.2 The Large Hadron Collider and the Compact Muon Solenoid

360 2.3 Muon Phase-II Upgrade

361 After the more than two years lasting First Long Shutdown (LS1), the Large Hadron Collider (LHC)
362 delivered its very first Run-II proton-proton collisions early 2015. LS1 gave the opportunity to the
363 LHC and to the its experiments to undergo upgrades. The accelerator is now providing collisions
364 at center-of-mass energy of 13 TeV and bunch crossing rate of 40 MHz, with a peak luminosity
365 exceeding its design value. During the first and upcoming second LHC Long Shutdown, the Compact
366 Muon Solenoid (CMS) detector is also undergoing a number of upgrades to maintain a high system
367 performance [1].

368 From the LHC Phase-2 or High Luminosity LHC (HL-LHC) period onwards, i.e. past the Third
369 Long Shutdown (LS3), the performance degradation due to integrated radiation as well as the average
370 number of inelastic collisions per bunch crossing, or pileup, will rise substantially and become a
371 major challenge for the LHC experiments, like CMS that are forced to address an upgrade program
372 for Phase-II [2]. Simulations of the expected distribution of absorbed dose in the CMS detector
373 under HL-LHC conditions, show in figure 5.14 that detectors placed close to the beamline will have
374 to withstand high irradiation, the radiation dose being of the order of a few tens of Gy.

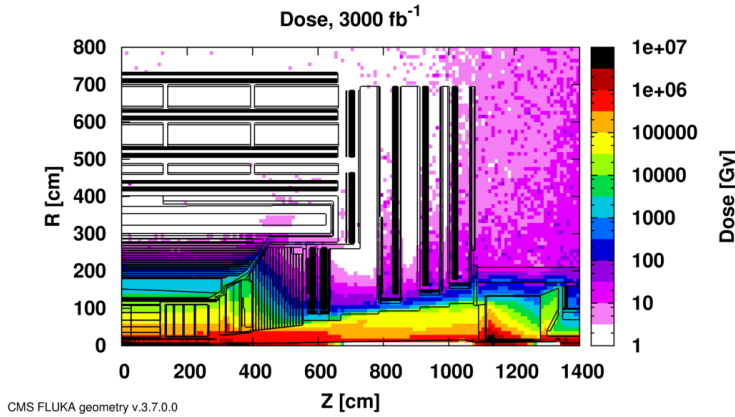


Figure 2.1: Absorbed dose in the CMS cavern after an integrated luminosity of 3000 fb⁻¹. R is the transverse distance from the beamline and Z is the distance along the beamline from the Interaction Point at Z=0.

The measurement of small production cross-section and/or decay branching ratio processes, such as the Higgs boson coupling to charge leptons or the $B_s \rightarrow \mu^+\mu^-$ decay, is of major interest and specific upgrades in the forward regions of the detector will be required to maximize the physics acceptance on the largest possible solid angle. To ensure proper trigger performance within the present coverage, the muon system will be completed with new chambers. In figure 2.2 one can see that the existing Cathode Strip Chambers (CSCs) will be completed by Gas Electron Multipliers (GEMs) and Resistive Plate Chambers (RPCs) in the pseudo-rapidity region $1.6 < |\eta| < 2.4$ to complete its redundancy as originally scheduled in the CMS Technical Proposal [3].

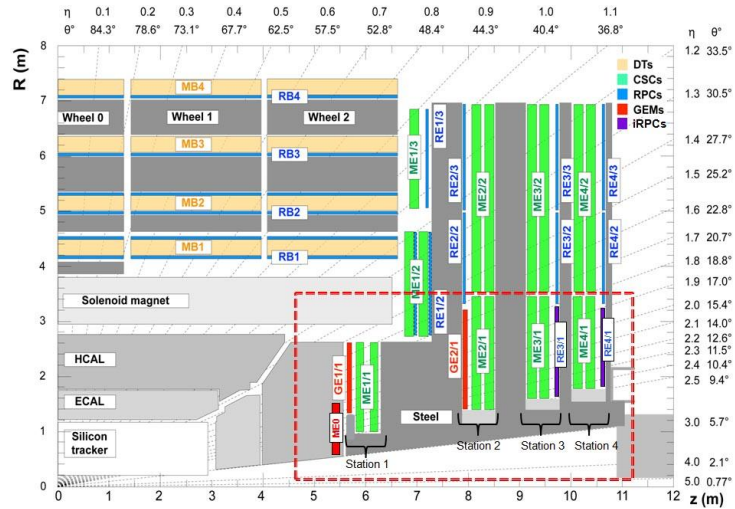


Figure 2.2: A quadrant of the muon system, showing DTs (yellow), RPCs (light blue), and CSCs (green). The locations of new forward muon detectors for Phase-II are contained within the dashed box and indicated in red for GEM stations (ME0, GE1/1, and GE2/1) and dark blue for improved RPC (iRPC) stations (RE3/1 and RE4/1).

RPCs are used by the CMS first level trigger for their good timing performances. Indeed, a very

good bunch crossing identification can be obtained with the present CMS RPC system, given their fast response of the order of 1 ns. In order to contribute to the precision of muon momentum measurements, muon chambers should have a spatial resolution less or comparable to the contribution of multiple scattering [1]. Most of the plausible physics is covered only considering muons with $p_T < 100$ GeV thus, in order to match CMS requirements, a spatial resolution of $\mathcal{O}(\text{few mm})$ the proposed new RPC stations, as shown by the simulation in figure 2.3. According to preliminary designs, RE3/1 and RE4/1 readout pitch will be comprised between 3 and 6 mm and 5 η -partitions could be considered.

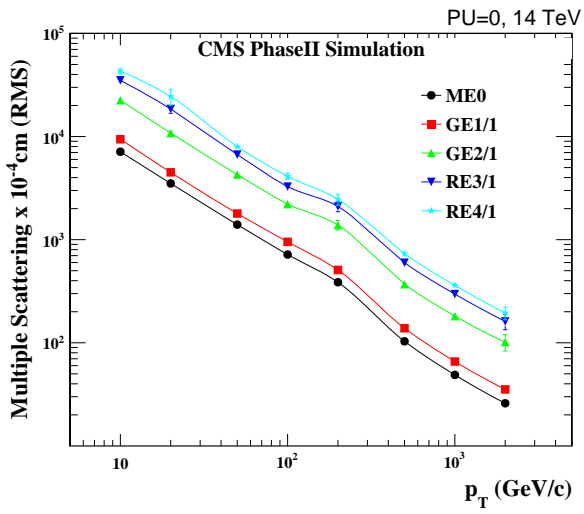


Figure 2.3: RMS of the multiple scattering displacement as a function of muon p_T for the proposed forward muon stations. All of the electromagnetic processes such as bremsstrahlung and magnetic field effect are included in the simulation.

3

392

Amplification processes in gaseous detectors

394 **3.1 Signal formation**

395 **3.2 Gas transport parameters**

4

396

397

Resistive Plate Chambers

398 **4.1 Principle**

399 **4.2 Rate capability of Resistive Plate Chambers**

400 **4.3 High time resolution**

401 **4.4 Resistive Plate Chambers at CMS**

402 **4.4.1 Overview**

403 The Resistive Plate Chambers (RPC) system, located in both barrel and endcap regions, provides a
404 fast, independent muon trigger with a looser p_T threshold over a large portion of the pseudorapidity
405 range ($|\eta| < 1.6$) [add reconstruction].

406

407 During High-Luminosity LHC (HL-LHC) operations the expected conditions in terms of back-
408 ground and pile-up will make the identification and correct P_T assignment a challenge for the Muon
409 system. The goal of RPC upgrade is to provide additional hits to the Muon system with precise tim-
410 ing. All these informations will be elaborated by the trigger system in a global way enhancing the
411 performance of the trigger in terms of efficiency and rate control. The RPC Upgrade is based on two
412 projects: an improved Link Board System and the extension of the RPC coverage up to $|\eta| = 2.4$.
413 [FIXME 2.4 or 2.5?]

414 The Link Board system, that will be described in section xxx, is responsible to process, syn-
415 chronize and zero-suppress the signals coming from the RPC front end boards. The Link Board
416 components have been produced between 2006 and 2007 and will be subjected to aging and failure
417 in the long term. The upgraded Link Board system will overcome the aging problems described in
418 section xxx and will allow for a more precise timing information to the RPC hits from 25 to 1 ns [ref
419 section xxx].

420 The extension of the RPC system up to $|\eta| = 2.1$ was already planned in the CMS TDR [ref
 421 cmstdr] and staged because of budget limitations and expected background rates higher than the rate
 422 capability of the present CMS RPCs in that region. An extensive R&D program has been done in
 423 order to develop an improved RPC that fulfills the CMS requirements. Two new RPC layers in the
 424 innermost ring of stations 3 and 4 will be added with benefits to the neutron-induced background
 425 reduction and efficiency improvement for both trigger and offline reconstruction.

426 4.4.2 The present RPC system

427 The RPC system is organized in 4 stations called RB1 to RB4 in the barrel region, and RE1 to RE4
 428 in the endcap region. The innermost barrel stations, RB1 and RB2, are instrumented with 2 layers
 429 of RPCs facing the innermost (RB1in and RB2in) and outermost (RB1out and RB2out) sides of the
 430 DT chambers. Every chamber is then divided from the read-out point of view into 2 or 3 η partitions
 431 called “rolls”. The RPC system consist of 480 barrel chambers and 576 endcap chambers. Details
 432 on the geometry are discussed in the paper [ref to geo paper].

433 The CMS RPC chamber is a double-gap, operated in avalanche mode to ensure reliable operation
 434 at high rates. Each RPC gap consists of two 2-mm-thick resistive High-Pressure Laminate (HPL)
 435 plates separated by a 2-mm-thick gas gap. The outer surface of the HPL plates is coated with a thin
 436 conductive graphite layer, and a voltage is applied. The RPCs are operated with a 3-component,
 437 non-flammable gas mixture consisting of 95.2% freon ($C_2H_2F_4$, known as R134a), 4.5% isobutane
 438 ($i-C_4H_{10}$), and 0.3% sulphur hexafluoride (SF_6) with a relative humidity of 40% - 50%. Readout
 439 strips are aligned in η between the 2 gas gaps. [\[Add a sentence on FEBs.\]](#)

440 The discriminated signals coming from the Front End boards feed via twisted cables (10 to 20 m
 441 long) the Link Board System located in UXC on the balconies around the detector. The Link System
 442 consist of the 1376 Link Boards (LBs) and the 216 Control Boards (CBs), placed in 108 Link Boxes.
 443 The Link Box is a custom crate (6U high) with 20 slots (for two CBs and eighteen LBs). The Link
 444 Box contains custom backplane to which the cables from the chambers are connected, as well as the
 445 cables providing the LBs and CBs power supply and the cables for the RPC FEBs control with use
 446 of the I2C protocol (trough the CB). The backplane itself contains only connectors (and no any other
 447 electronic devices).

448 The Link Board has 96 input channels (one channel corresponds to one RPC strip). The input
 449 signals are the ~ 100 ns binary pulses which are synchronous to the RPC hits, but not to the LHC
 450 clock (which drives the entire CMS electronics). Thus the first step of the FEB signals processing
 451 is synchronization, i.e. assignment of the signals to the BXes (25 ns periods). Then the data are
 452 compressed with a simple zero-suppressing algorithm (the input channels are grouped into 8 bit
 453 partitions, only the partitions with at least one nonzero bit are selected for each BX). Next, the non-
 454 empty partitions are time-multiplexed i.e. if there are more than one such partition in a given BX,
 455 they are sent one-by-one in consecutive BXes. The data from 3 neighbouring LBs are concentrated
 456 by the middle LB which contains the optical transmitter for sending them to the USC over a fiber at
 457 1.6 Gbps.

458 The Control Boards provide the communication of the control software with the LBs via the
 459 FEC/CCU system. The CBs are connected into token rings, each ring consists of 12 CBs of one
 460 detector tower and a FEC mezzanine board placed on the CCS board located in the VME crate in
 461 the USC. In total, there are 18 rings in the entire Link System. The CBs also perform automatic
 462 reloading of the LB's firmware which is needed in order to avoid accumulation of the radiation
 463 induced SEUs in the LBs firmware.

464 Both LBs and CB are based on the Xilinx Spartan III FPGAs, the CB additionally contains
 465 radiation-tolerant (FLASH based) FPGA Actel ProAsicPlus.

466 The High Voltage power system is located in USC, not exposed to radiation and easily accessible
 467 for any reparation. A single HV channel powers 2 RPC chambers both in the barrel and endcap
 468 regions. The Low Voltage boards are located in UXC on the balconies and provide the voltage to the
 469 front end electronics.

470 4.4.3 Pulse processing of CMS RPCs

471 Signals induced by cosmic particle in the RPC strips are shaped by standard CMS RPC Front-End
 472 Electronics (FEE) following the scheme of Figure 4.1. On a first stage, analogic signals are amplified
 473 and then sent to the Constant Fraction Discriminator (CFD) described in Figure 4.2. At the end of
 474 the chain, 100 ns long pulses are sent in the LVDS output. These output signal are sent on one side to
 475 a V1190A Time-to-Digital Converter (TDC) module from CAEN and on the other to an OR module
 476 to count the number of detected signals. Trigger and hit coïncidences are monitored using scalers.
 477 The TDC is used to store the data into ROOT files. These files are thus analysed to understand the
 478 detectors performance.

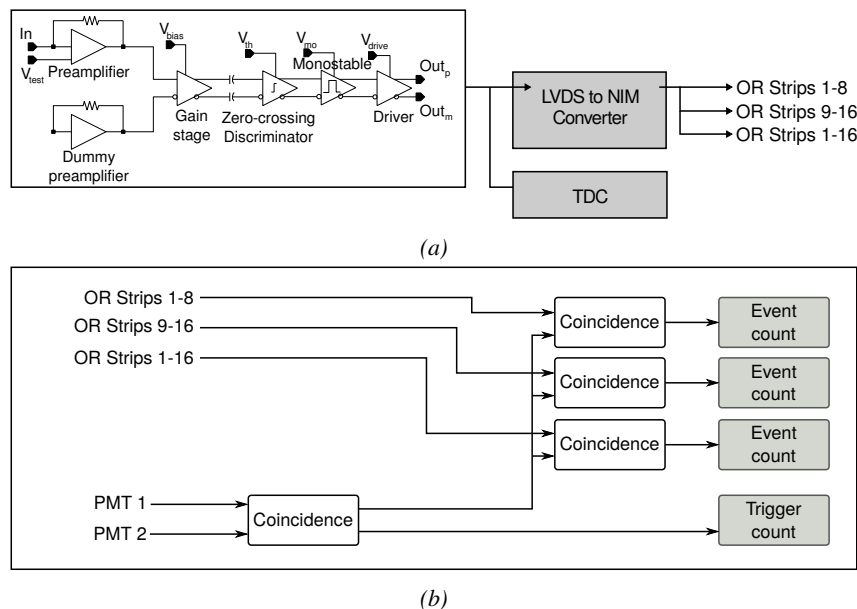


Figure 4.1: Signals from the RPC strips are shaped by the FEE described on Figure 4.1a. Output LVDS signals are then read-out by a TDC module connected to a computer or converted into NIM and sent to scalers. Figure 4.1b describes how these converted signals are put in coincidence with the trigger.

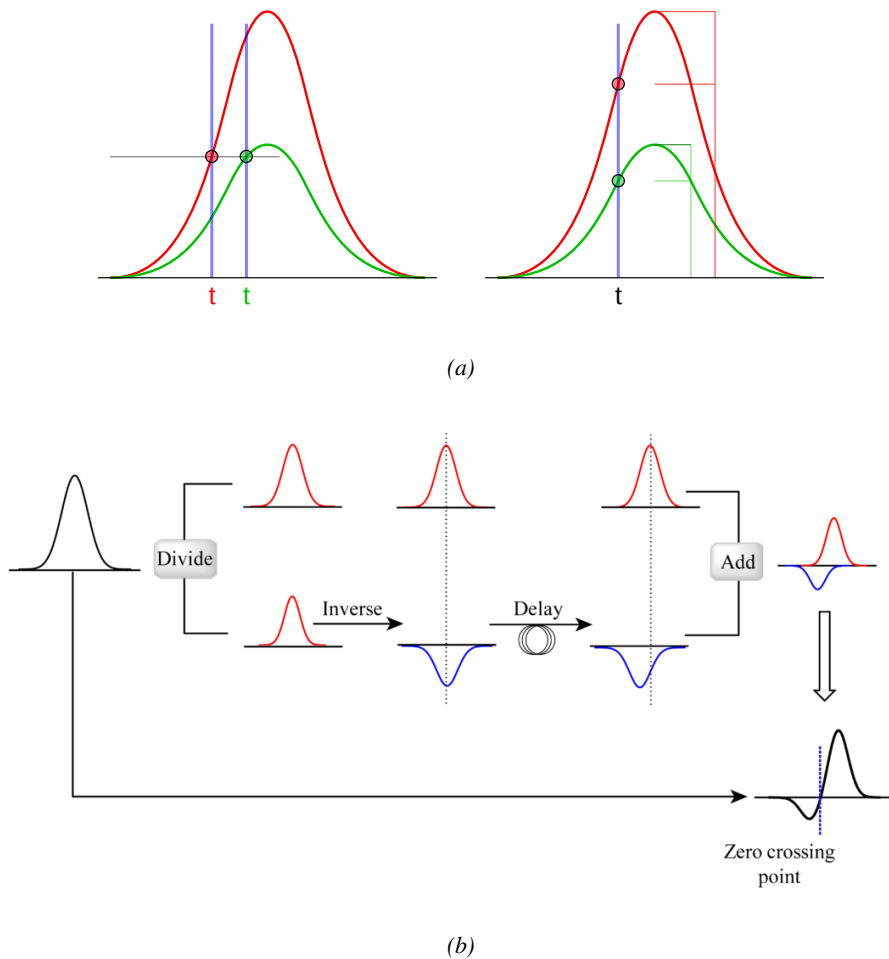


Figure 4.2: Description of the principle of a CFD. A comparison of threshold triggering (left) and constant fraction triggering (right) is shown in Figure 4.2a. Constant fraction triggering is obtained thanks to zero-crossing technique as explained in Figure 4.2b. The signal arriving at the input of the CFD is split into three components. A first one is delayed and connected to the inverting input of a first comparator. A second component is connected to the noninverting input of this first comparator. A third component is connected to the noninverting input of another comparator along with a threshold value connected to the inverting input. Finally, the output of both comparators is fed through an AND gate.

5

479

480
481

Longevity studies and Consolidation of the present CMS RPC subsystem

482

5.1 Testing detectors under extreme conditions

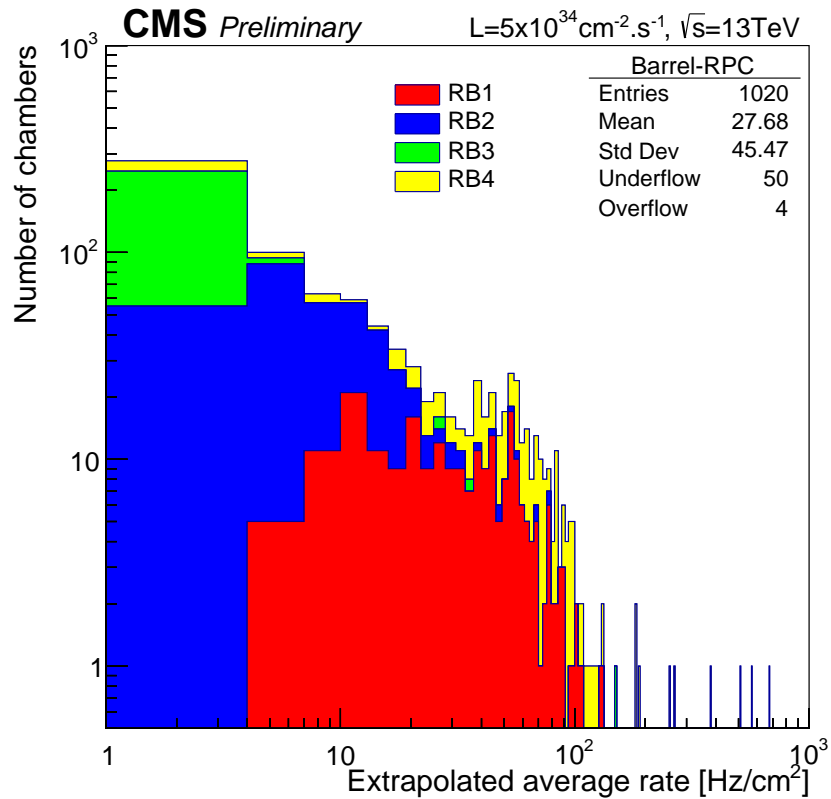
483
484
485
486
487
488
489
490

The upgrade from LHC to HL-LHC will increase the peak luminosity from $10^{34} \text{ cm}^{-2} \text{ s}^{-1}$ to reach $5 \times 10^{34} \text{ cm}^{-2} \text{ s}^{-1}$, increasing in the same way the total expected background to which the RPC system will be subjected to. Composed of low energy gammas and neutrons from $p\text{-}p$ collisions, low momentum primary and secondary muons, puch-through hadrons from calorimeters, and particles produced in the interaction of the beams with collimators, the background will mostly affect the regions of CMS that are the closest to the beam line, i.e. the RPC detectors located in the endcaps.

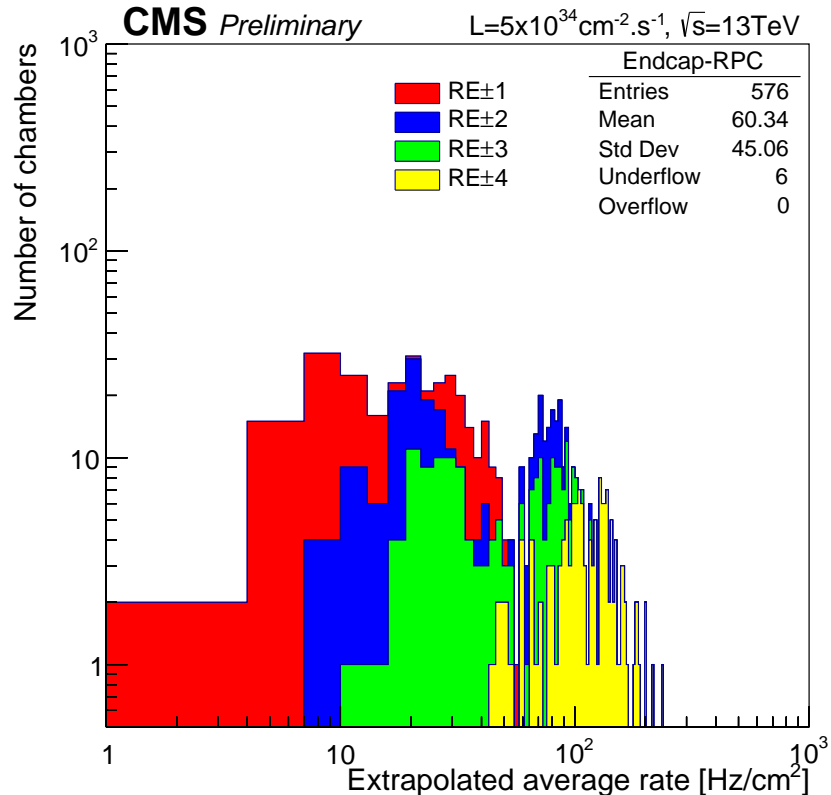
[To update.]

491
492
493
494
495
496
497
498
499

The 2016 data allowed to study the values of the background rate in all RPC system. In Figure 5.1, the distribution of the chamber background hit rate per unit area is shown at a luminosity of $5 \times 10^{34} \text{ cm}^{-2} \cdot \text{s}^{-1}$ linearly extrapolating from data collected in 2016 [ref mentioning the linear dependency of rate vs lumi]. The maximum rate per unit area at HL-LHC conditions is expected to be of the order of 600 Hz/cm^2 (including a safety factor 3). Nevertheless, Fluka simulations have conducted in order to understand the background at HL-LHC conditions. The comparison to the data has shown, in Figure 5.2, a discrepancy of a factor 2 even though the order of magnitude is consistent. [Understand mismatch.]



(a)



(b)

Figure 5.1: (5.1a) Extrapolation from 2016 data of single hit rate per unit area in the barrel region. (5.1b) Extrapolation from 2016 data of single hit rate per unit area in the endcap region.

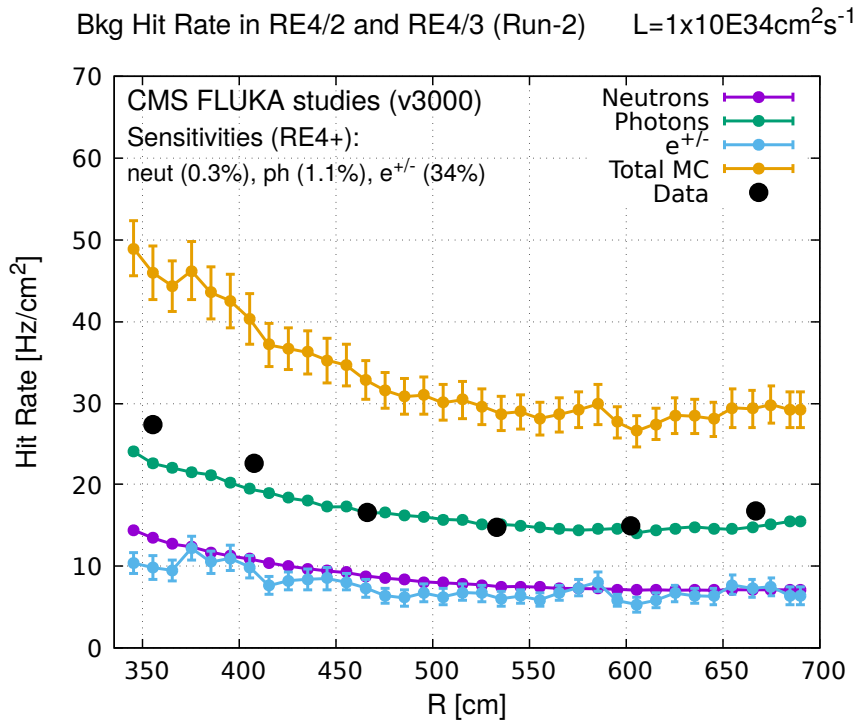


Figure 5.2: Background Fluka simulation compared to 2016 Data at $L = 10^{34}\text{cm}^{-2}\cdot\text{s}^{-1}$ in the fourth endcap disk region. A mismatch in between simulation and data can be observed. [\[To be understood.\]](#)

500 In the past, extensive long-term tests were carried out at several gamma and neutron facilities
 501 certifying the detector performance. Both full size and small prototype RPCs have been irradiated
 502 with photons up to an integrated charge of $\sim 0.05\text{C}/\text{cm}^2$ and $\sim 0.4\text{C}/\text{cm}^2$, respectively [4, 5].
 503 During Run-I, the RPC system provided stable operation and excellent performance and did not
 504 show any aging effects for integrated charge of the order of $0.01\text{C}/\text{cm}^2$. Projections on currents
 505 from 2016 Data, has allowed to determine that the total integrated charge, by the end of HL-LHC,
 506 would be of the order of $1\text{C}/\text{cm}^2$ (including a safety factor 3). [\[Corresponding figure needed.\]](#)

507

508 5.1.1 The Gamma Irradiation Facilities

509 5.1.1.1 GIF

510 Located in the SPS West Area at the downstream end of the X5 test beam, the Gamma Irradiation
 511 Facility (GIF) was a test area in which particle detectors were exposed to a particle beam in presence
 512 of an adjustable gamma background [6]. Its goal was to reproduce background conditions these
 513 detectors would suffer in their operating environment at LHC. GIF layout is shown in Figure 5.3.
 514 Gamma photons are produced by a strong ^{137}Cs source installed in the upstream part of the zone
 515 inside a lead container. The source container includes a collimator, designed to irradiate a $6 \times 6\text{ m}^2$
 516 area at 5 m maximum to the source. A thin lens-shaped lead filter helps providing with a uniform
 517 outcoming flux in a vertical plane, orthogonal to the beam direction. The principal collimator hole
 518 provides a pyramidal aperture of $74^\circ \times 74^\circ$ solid angle and provides a photon flux in a pyramidal vol-

ume along the beam axis. The photon rate is controled by further lead filters allowing the maximum rate to be limited and to vary within a range of four orders of magnitude. Particle detectors under test are then placed within the pyramidal volume in front of the source, perpendicularly to the beam line in order to profit from the homogeneous photon flux. Adjusting the background flux of photons can then be done by using the filters and choosing the position of the detectors with respect to the source.

524

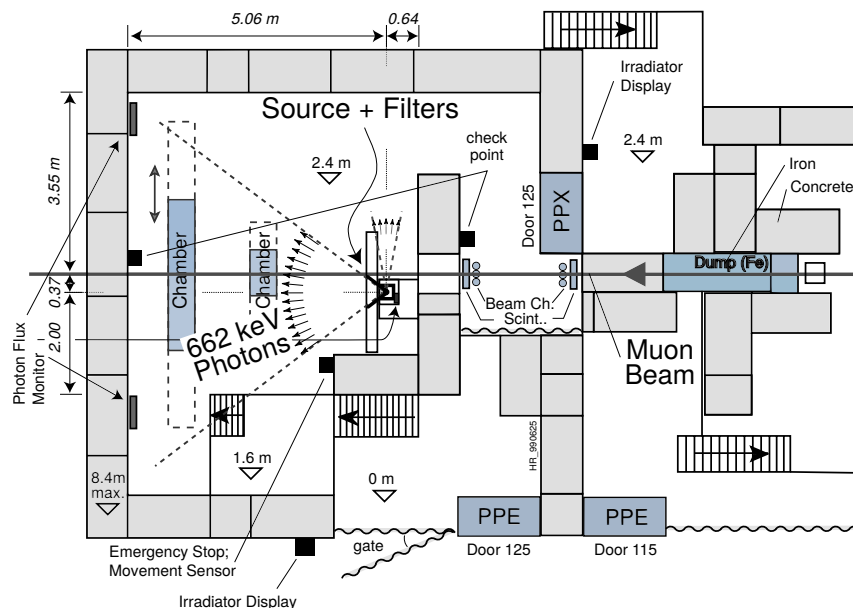


Figure 5.3: Layout of the test beam zone called X5c GIF at CERN. Photons from the radioactive source produce a sustained high rate of random hits over the whole area. The zone is surrounded by 8 m high and 80 cm thick concrete walls. Access is possible through three entry points. Two access doors for personnel and one large gate for material. A crane allows installation of heavy equipment in the area.

As described on Figure 5.4, the ^{137}Cs source emits a 662 keV photon in 85% of the decays. An activity of 740 GBq was measured on the 5th March 1997. To estimate the strength of the flux in 2014, it is necessary to consider the nuclear decay through time assiciated to the Cesium source whose half-life is well known ($t_{1/2} = (30.05 \pm 0.08)$ y). The GIF tests where done in between the 20th and the 31st of August 2014, i.e. at a time $t = (17.47 \pm 0.02)$ y resulting in an attenuation of the activity from 740 GBq in 1997 to 494 GBq in 2014.

531

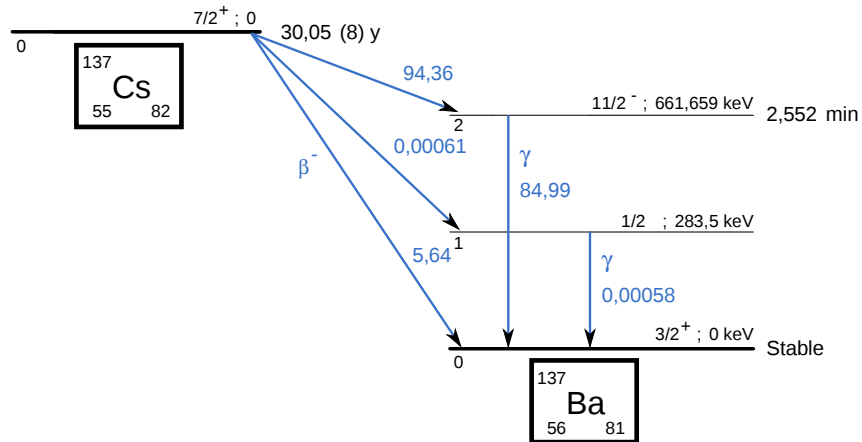


Figure 5.4: ^{137}Cs decays by β^- emission to the ground state of ^{137}Ba ($BR = 5.64\%$) and via the 662 keV isomeric level of ^{137}Ba ($BR = 94.36\%$) whose half-life is 2.55 min.

5.1.1.2 GIF++

The new Gamma Irradiation Facility (GIF++), located in the SPS North Area at the downstream end of the H4 test beam, has replaced its predecessor during LS1 and has been operational since spring 2015 [7]. Like GIF, GIF++ features a ^{137}Cs source of 662 keV gamma photons, their fluence being controlled with a set of filters of various attenuation factors. The source provides two separated large irradiation areas for testing several full-size muon detectors with continuous homogeneous irradiation, as presented in Figure 5.5.

539

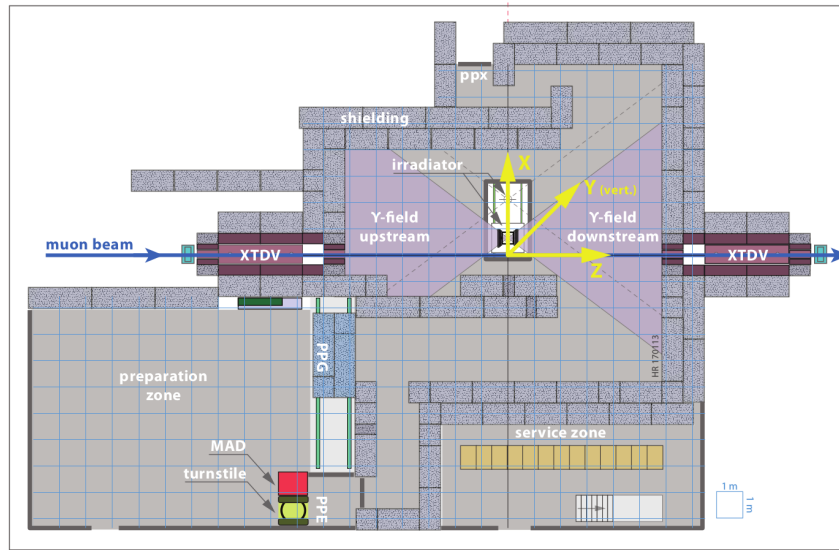


Figure 5.5: Floor plan of the GIF++ facility. When the facility downstream of the GIF++ takes electron beam, a beam pipe is installed along the beam line (z -axis). The irradiator can be displaced laterally (its center moves from $x = 0.65$ m to 2.15 m), to increase the distance to the beam pipe.

540 The source activity was measured to be about 13.5 TBq in March 2016. The photon flux being
 541 far greater than HL-LHC expectations, GIF++ provides an excellent facility for accelerated aging
 542 tests of muon detectors.

543

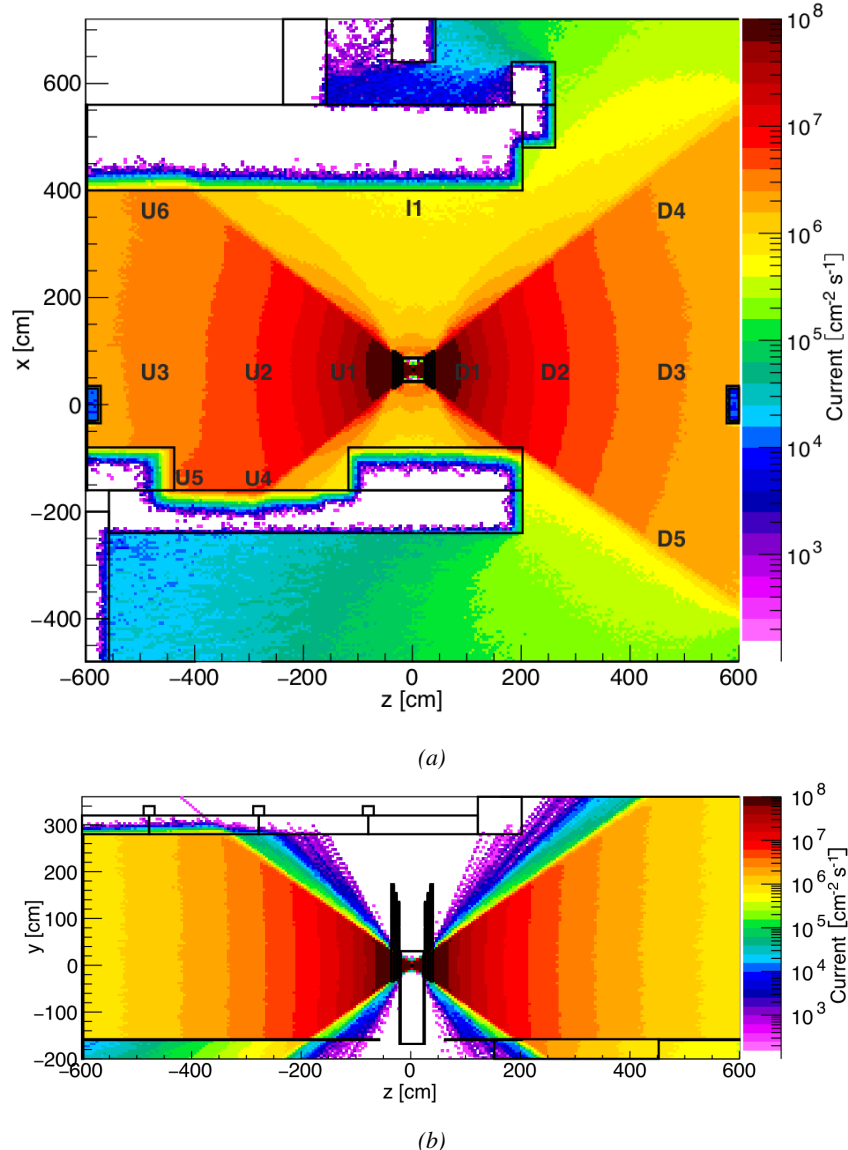


Figure 5.6: Simulated unattenuated current of photons in the xz plane (Figure 5.6a) and yz plane (Figure 5.6b) through the source at $x = 0.65$ m and $y = 0$ m. With angular correction filters, the current of 662 keV photons is made uniform in xy planes.

544 The source is situated in the muon beam line with the muon beam being available a few times a
 545 year. The H4 beam, composed of muons with a momentum of about 150 GeV/c, passes through the
 546 GIF++ zone and is used to study the performance of the detectors. Its flux is of 104 particles/ s cm^2

547 focused in an area similar to $10 \times 10 \text{ cm}^2$. Therefore, with properly adjusted filters, one can imitate
 548 the HL-LHC background and study the performance of muon detectors with their trigger/readout
 549 electronics in HL-LHC environment.

550

551 5.2 Preliminary tests at GIF

552 5.2.1 Resistive Plate Chamber test setup

553 During summer 2014, preliminary tests have been conducted in the GIF area on a newly produced
 554 RE4/2 chamber labelled RE-4-2-BARC-161. This chamber has been placed into a trolley covered
 555 with a tent. The position of the RPC inside the tent and of the tent related to the source is described
 556 in Figure 5.7. To test this CMS RPC, three different absorber settings were used. First of all,
 557 measurements were done with fully opened source. Then, to complete this preliminary study, the
 558 gamma flux has been attenuated from a factor 2 and a factor 5. The expected gamma flux at the level
 559 of our detector will be discussed in subsection 5.2.4.

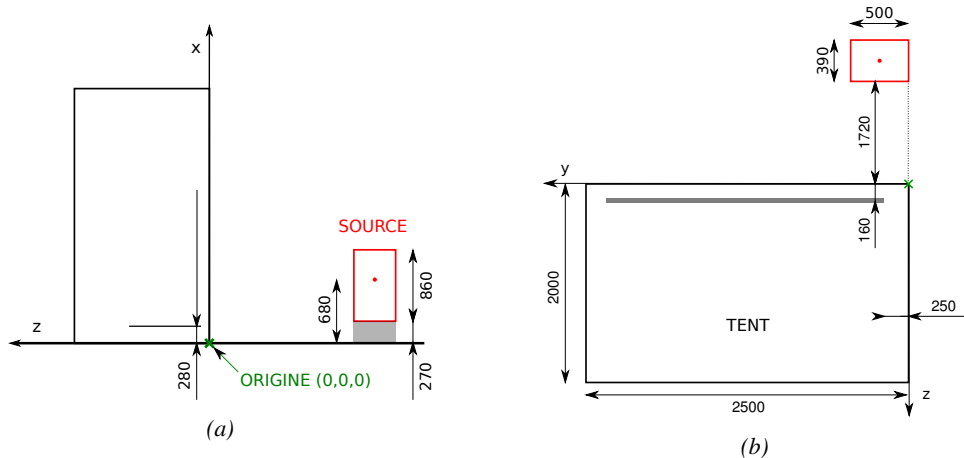


Figure 5.7: Description of the RPC setup. Dimensions are given in mm. A tent containing RPCs is placed at 1720 mm from the source container. The source is situated in the center of the container. RE-4-2-BARC-161 chamber is 160 mm inside the tent. This way, the distance between the source and the chambers plan is 2060 mm. Figure 5.7a provides a side view of the setup in the xz plane while Figure 5.7b shows a top view in the yz plane.



Figure 5.8: RE-4-2-BARC-161 chamber is inside the tent as described in Figure 5.7. In the top right, the two scintillators used as trigger can be seen. This trigger system has an inclination of 10° relative to horizontal and is placed above half-partition B2 of the RPCs. PMT electronics are shielded thanks to lead blocks placed in order to protect them without stopping photons from going through the scintillators and the chamber.

560 At the time of the tests, the beam not being operational anymore, a trigger composed of 2
 561 plastic scintillators has been placed in front of the setup with an inclination of 10 deg with respect to
 562 the detector plane in order to look at cosmic muons. Using this particular trigger layout, shown on
 563 Figure 5.8, leads to a cosmic muon hit distribution into the chamber similar to the one in Figure 5.9.
 564 Measured without gamma irradiation, two peaks can be seen on the profil of partition B, centered on
 565 strips 52 and 59. Section 5.2.3 will help us understand that these two peaks are due respectively to
 566 forward and backward coming cosmic particles where forward coming particles are first detected by
 567 the scintillators and then the RPC while the backward coming muons are first detected in the RPC.

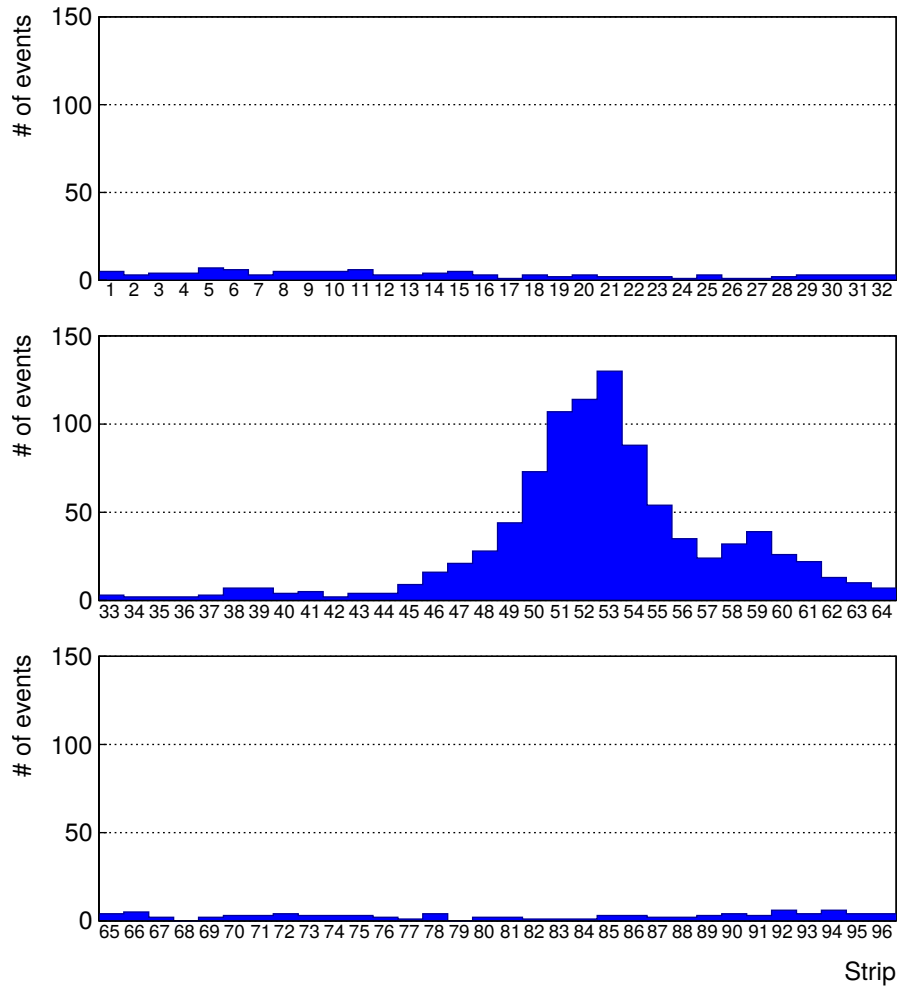


Figure 5.9: Hit distributions over all 3 partitions of RE-4-2-BARC-161 chamber is showed on these plots. Top, middle and bottom figures respectively correspond to partitions A, B, and C. These plots show that some events still occur in other half-partitions than B2, which corresponds to strips 49 to 64, in front of which the trigger is placed, contributing to the inefficiency of detection of cosmic muons. In the case of partitions A and C, the very low amount of data can be interpreted as noise. On the other hand, it is clear that a little portion of muons reach the half-partition B1, corresponding to strips 33 to 48.

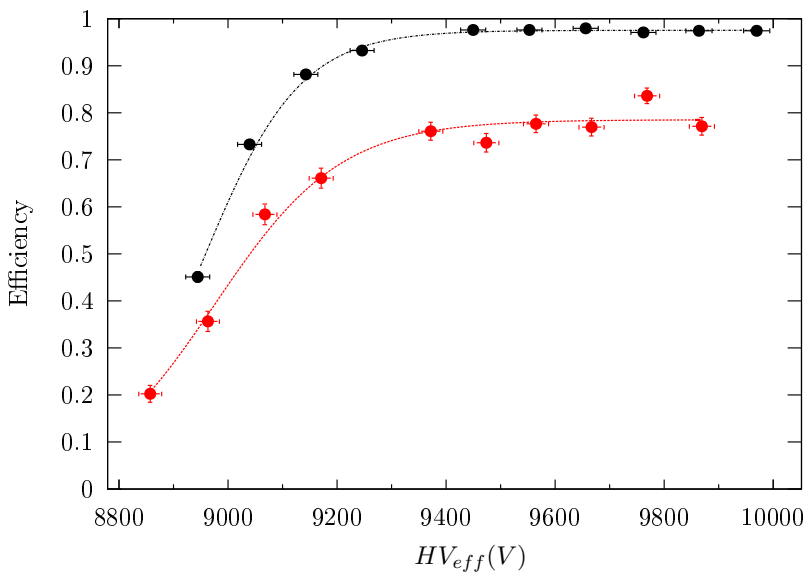
568 5.2.2 Data Acquisition

569 5.2.3 Geometrical acceptance of the setup layout to cosmic muons

570 In order to profit from a constant gamma irradiation, the detectors inside of the GIF bunker need
 571 to be placed in a plane orthogonal to the beam line. The muon beam that used to be available was
 572 meant to test the performance of detectors under test. This beam not being active anymore, another
 573 solution to test detector performance had to be used. Thus, it has been decided to use cosmic muons
 574 detected through a telescope composed of two scintillators. Lead blocks were used as shielding to

575 protect the photomultipliers from gammas as can be seen from Figure 5.8.

576 An inclination has been given to the cosmic telescope to maximize the muon flux. A good com-
 577 promise had to be found between good enough muon flux and narrow enough hit distribution to
 578 be sure to contain all the events into only one half partitions as required from the limited available
 579 readout hardware. Nevertheless, a consequence of the misplaced trigger, that can be seen as a loss
 580 of events in half-partition B1 in Figure 5.9, is an inefficiency. Nevertheless, the inefficiency of ap-
 581 proximately 20 % highlighted in Figure 5.10 by comparing the performance of chamber BARC-161
 582 in 904 and at GIF without irradiation seems too important to be explained only by the geometri-
 583 cal acceptance of the setup itself. Simulations have been conducted to show how the setup brings
 584 inefficiency.



585 *Figure 5.10: Results are derived from data taken on half-partition B2 only. On the 18th of June 2014, data
 586 has been taken on chamber RE-2-BARC-161 at building 904 (Prevessin Site) with cosmic muons providing us a
 587 reference efficiency plateau of $(97.54 \pm 0.15)\%$ represented by a black curve. A similar measurement has been
 588 done at GIF on the 21st of July with the same chamber giving a plateau of $(78.52 \pm 0.94)\%$ represented by a
 589 red curve.*

585 5.2.3.1 Description of the simulation layout

586 The layout of GIF setup has been reproduced and incorporated into a Monte Carlo (MC) simulation
 587 to study the influence of the disposition of the telescope on the final distribution measured by the
 588 RPC. A 3D view of the simulated layout is given into Figure 5.11. Muons are generated randomly
 589 in a horizontal plane located at a height corresponding to the lowest point of the PMTs. This way,
 590 the needed size of the plane in order to simulate events happening at very big azimuthal angles (i.e.
 591 $\theta \approx \pi$) can be kept relatively small. The muon flux is designed to follow the usual $\cos^2\theta$ distribution
 592 for cosmic particle. The goal of the simulation is to look at muons that pass through the muon
 593 telescope composed of the two scintillators and define their distribution onto the RPC plane. During
 594 the reconstruction, the RPC plane is then divided into its strips and each muon track is assigned to a
 595 strip.

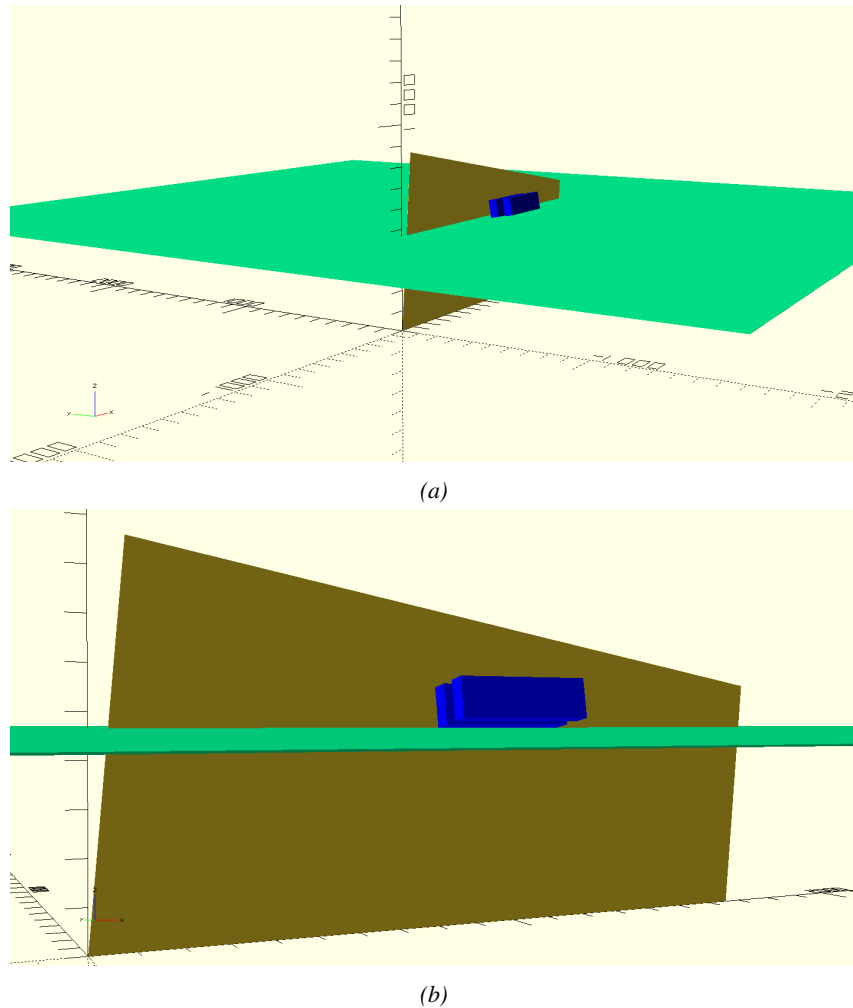


Figure 5.11: Representation of the layout used for the simulations of the test setup. The RPC is represented as a yellow trapezoid while the two scintillators as blue cuboids looking at the sky. A green plane corresponds to the muon generation plane within the simulation. Figure 5.7a shows a global view of the simulated setup. Figure 5.7b shows a zoomed view that allows to see the 2 scintillators as well as the full RPC plane.

596 In order to further refine the quality of the simulation and understand deeper the results the
 597 dependance of the distribution has been studied for a range of telescope inclinations. Moreover,
 598 the threshold applied on the PMT signals has been included into the simulation in the form of a
 599 cut. In the approximation of uniform scintillators, it has been considered that the threshold can be
 600 understood as the minimum distance particles need to travel through the scintillating material to give
 601 a strong enough signal. Particles that travel a distance smaller than the set "threshold" are thus not
 602 detected by the telescope and cannot trigger the data taking. Finally, the FEE threshold also has
 603 been considered in a similar way. The mean momentum of horizontal cosmic rays is higher than
 604 those of vertical ones but the stopping power of matter for momenta ranging from 1 GeV to 1 TeV
 605 stays comparable. It is then possible to assume that the mean number of primary e^-/ion pairs per
 606 unit length will stay similar and thus, depending on the applied discriminator threshold, muons with

607 the shortest path through the gas volume will deposit less charge and induce a smaller signal on the
 608 pick-up strips that could eventually not be detected. These two thresholds also restrain the overall
 609 geometrical acceptance of the system.

610 **5.2.3.2 Simulation procedure**

611 The simulation software has been designed using C++ and the output data is saved into ROOT
 612 histograms. Simulations start for a threshold T_{scint} varying in a range from 0 to 45 mm in steps
 613 of 5 mm, where $T_{scint} = 0$ mm corresponds to the case where there isn't any threshold apply on
 614 the input signal while $T_{scint} = 45$ mm, which is the scintillator thickness, is the case where muons
 615 cannot arrive orthogonally onto the scintillator surface. For a given T_{scint} , a set of RPC thresholds
 616 are considered. The RPC threshold, T_{RPC} varies from 2 mm, the thickness of the gas volume, to
 617 3 mm in steps of 0.25 mm. For each $(T_{scint}; T_{RPC})$ pair, $N_\mu = 10^8$ muons are randomly generated
 618 inside the muon plane described in the previous paragraph with an azimuthal angle θ chosen to follow
 619 a $\cos^2\theta$ distribution.

620 Planes are associated to each surface of the scintillators. Knowing muon position into the muon
 621 plane and its direction allows us, by assuming that muons travel in a straight line, to compute the
 622 intersection of the muon track with these planes. Applying conditions to the limits of the surfaces
 623 of the scintillator faces then gives us an answer to whether or not the muon passed through the
 624 scintillators. In the case the muon has indeed passed through the telescope, the path through each
 625 scintillator is computed and muons whose path was shorter than T_{scint} are rejected and are thus
 626 considered as having not interacted with the setup.

627 On the contrary, if the muon is labeled as good, its position within the RPC plane is computed
 628 and the corresponding strip, determined by geometrical tests in the case the distance through the
 629 gas volume was enough not to be rejected because of T_{RPC} , gets a hit and several histograms
 630 are filled in order to keep track of the generation point on the muon plane, the intersection points
 631 of the reconstructed muons within the telescope, or on the RPC plane, the path traveled through
 632 each individual scintillator or the gas volume, as well as other histograms. Moreover, muons fill
 633 different histograms whether they are forward or backward coming muons. They are discriminated
 634 according to their direction components. When a muon is generated, an (x, y, z) position is assigned
 635 into the muon plane as well as a $(\theta; \phi)$ pair that gives us the direction it's coming from. This way,
 636 muons satisfying the condition $0 \leq \phi < \pi$ are designated as backward coming muons while muons
 637 satisfying $\pi \leq \phi < 2\pi$ as forward coming muons.

638 This simulation is then repeated for different telescope inclinations ranging in between 4 and 20°
 639 and varying in steps of 2° . Due to this inclination and to the vertical position of the detector under
 640 test, the muon distribution reconstructed in the detector plane is asymmetrical. The choice as been
 641 made to chose a skew distribution formula to fit the data built as the multiplication of gaussian and
 642 sigmoidal curves together. A typical gaussian formula is given as 5.1 and has three free parameters
 643 as A_g , its amplitude, \bar{x} , its mean value and σ , its root mean square. Sigmoidal curves as given by
 644 formula 5.2 are functions converging to 0 and A_s as x diverges. The inflection point is given as x_i
 645 and λ is proportional to the slope at $x = x_i$. In the limit where $\lambda \rightarrow \infty$, the sigmoid becomes a
 646 step function.

$$g(x) = A_g e^{-\frac{(x-\bar{x})^2}{2\sigma^2}} \quad (5.1)$$

$$s(x) = \frac{A_s}{1 + e^{-\lambda(x-x_i)}} \quad (5.2)$$

Finally, a possible representation of a skew distribution is given by formula 5.3 and is the product of 5.1 and 5.2. Naturally, here $A_{sk} = A_g \times A_s$ and represents the theoretical maximum in the limit where the skew tends to a gaussian function.

$$sk(x) = g(x) \times s(x) = A_{sk} \frac{e^{\frac{-(x-\bar{x})^2}{2\sigma^2}}}{1 + e^{-\lambda(x-x_i)}} \quad (5.3)$$

5.2.3.3 Results

Influence of T_{scint} on the muon distribution

Influence of T_{RPC} on the muon distribution

Influence of the telescope inclination on the muon distribution

Comparison to data taken at GIF without irradiation

5.2.4 Photon flux at GIF

5.2.4.1 Expectations from simulations

In order to understand and evaluate the γ flux in the GIF area, simulations had been conducted in 1999 and published by S. Agosteo et al [6]. Table 5.1 presented in this article gives us the γ flux for different distances D to the source. This simulation was done using GEANT and a Monte Carlo N-Particle (MCNP) transport code, and the flux F is given in number of γ per unit area and unit time along with the estimated error from these packages expressed in %.

Nominal ABS	Photon flux F [$s^{-1}cm^{-2}$]			
	at $D = 50$ cm	at $D = 155$ cm	at $D = 300$ cm	at $D = 400$ cm
1	$0.12 \cdot 10^8 \pm 0.2\%$	$0.14 \cdot 10^7 \pm 0.5\%$	$0.45 \cdot 10^6 \pm 0.5\%$	$0.28 \cdot 10^6 \pm 0.5\%$
2	$0.68 \cdot 10^7 \pm 0.3\%$	$0.80 \cdot 10^6 \pm 0.8\%$	$0.25 \cdot 10^6 \pm 0.8\%$	$0.16 \cdot 10^6 \pm 0.6\%$
5	$0.31 \cdot 10^7 \pm 0.4\%$	$0.36 \cdot 10^6 \pm 1.2\%$	$0.11 \cdot 10^6 \pm 1.2\%$	$0.70 \cdot 10^5 \pm 0.9\%$

Table 5.1: Total photon flux ($E\gamma \leq 662$ keV) with statistical error predicted considering a ^{137}Cs activity of 740 GBq at different values of the distance D to the source along the x -axis of irradiation field [6].

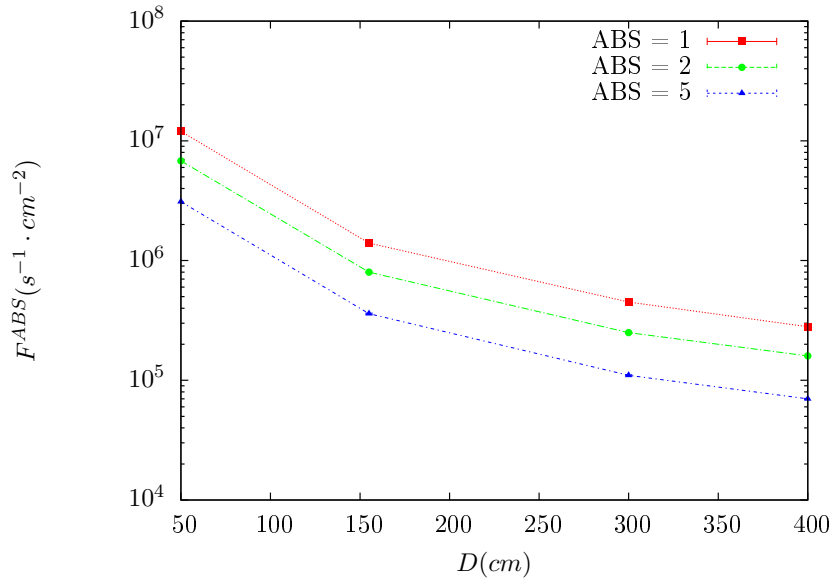


Figure 5.12: γ flux $F(D)$ is plot using values from table 5.1. As expected, the plot shows similar attenuation behaviours with increasing distance for each absorption factors.

The simulation doesn't directly provides us with an estimated flux at the level of our RPC. First of all, it is needed to extract the value of the flux from the available data contained in the original paper and then to estimate the flux in 2014 at the time the experimentation took place. Figure 5.12 that contains the data from Table 5.1. In the case of a pointlike source emitting isotropic and homogeneous gamma radiations, the gamma flux F at a distance D to the source with respect to a reference point situated at D_0 where a known flux F_0 is measured will be expressed like in Equation 5.4, assuming that the flux decreases as $1/D^2$, where c is a fitting factor.

$$F^{ABS} = F_0^{ABS} \times \left(\frac{cD_0}{D} \right)^2 \quad (5.4)$$

By rewriting Equation 5.4, it comes that :

$$c = \frac{D}{D_0} \sqrt{\frac{F^{ABS}}{F_0^{ABS}}} \quad (5.5)$$

$$\Delta c = \frac{c}{2} \left(\frac{\Delta F^{ABS}}{F^{ABS}} + \frac{\Delta F_0^{ABS}}{F_0^{ABS}} \right) \quad (5.6)$$

Finally, using Equation 5.5 and the data in Table 5.1 with $D_0 = 50$ cm as reference point, we can build Table 5.2. It is interesting to note that c for each value of D doesn't depend on the absorption factor.

Nominal ABS	Correction factor c		
	at $D = 155$ cm	at $D = 300$ cm	at $D = 400$ cm
1	$1.059 \pm 0.70\%$	$1.162 \pm 0.70\%$	$1.222 \pm 0.70\%$
2	$1.063 \pm 1.10\%$	$1.150 \pm 1.10\%$	$1.227 \pm 0.90\%$
5	$1.056 \pm 1.60\%$	$1.130 \pm 1.60\%$	$1.202 \pm 1.30\%$

Table 5.2: Correction factor c is computed thanks to formulae 5.5 taking as reference $D_0 = 50$ cm and the associated flux F_0^{ABS} for each absorption factor available in table 5.1.

673 For the range of D/D_0 values available, it is possible to use a simple linear fit to get the evolution
 674 of c . The linear fit will then use only 2 free parameters, a and b , as written in Equation 5.7. This gives
 675 us the results showed in Figure 5.13. Figure 5.13b confirms that using only a linear fit to extract c is
 676 enough as the evolution of the rate that can be obtained superimposes well on the simulation points.

$$c \left(\frac{D}{D_0} \right) = a \frac{D}{D_0} + b \quad (5.7)$$

$$F^{ABS} = F_0^{ABS} \left(a + \frac{bD_0}{D} \right)^2 \quad (5.8)$$

$$\Delta F^{ABS} = F^{ABS} \left[\frac{\Delta F_0^{ABS}}{F_0^{ABS}} + 2 \frac{\Delta a + \Delta b \frac{D_0}{D}}{a + \frac{bD_0}{D}} \right] \quad (5.9)$$

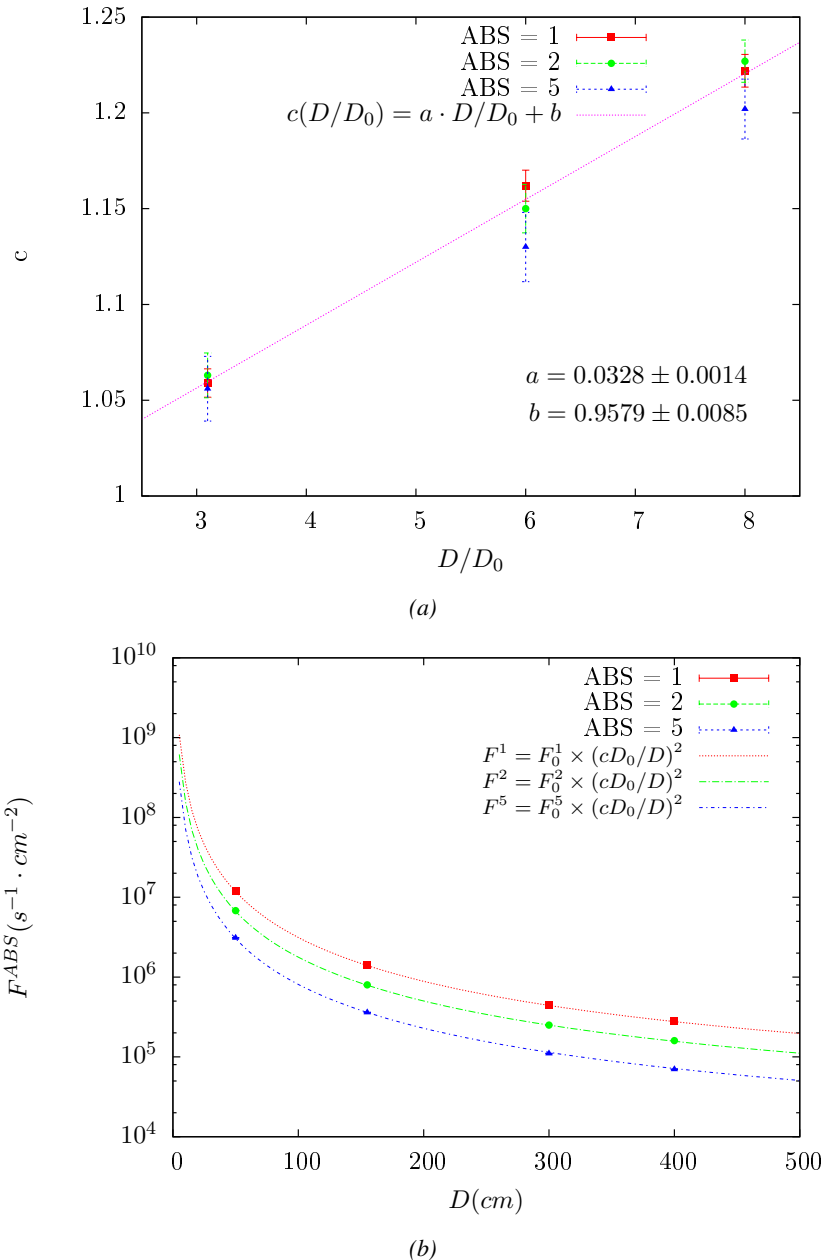


Figure 5.13: Figure 5.13a shows the linear approximation fit done via formulae 5.7 on data from table 5.2. Figure 5.13b shows a comparison of this model with the simulated flux using a and b given in figure 5.13a in formulae 5.4 and the reference value $D_0 = 50\text{cm}$ and the associated flux for each absorption factor F_0^{ABS} from table 5.1

In the case of the 2014 GIF tests, the RPC plane is located at a distance $D = 206\text{ cm}$ to the source.
 Moreover, to estimate the strength of the flux in 2014, it is necessary to consider the nuclear decay through time associated to the Cesium source whose half-life is well known ($t_{1/2} = (30.05 \pm 0.08)\text{ y}$).
 The very first source activity measurement has been done on the 5th of March 1997 while the GIF

681 tests where done in between the 20th and the 31st of August 2014, i.e. at a time $t = (17.47 \pm 0.02)$ y
 682 resulting in an attenuation of the activity from 740 GBq in 1997 to 494 GBq in 2014. All the needed
 683 information to extrapolate the flux through our detector in 2014 has now been assembled, leading
 684 to the Table 5.3. It is interesting to note that for a common RPC sensitivity to γ of $2 \cdot 10^{-3}$, the
 685 order of magnitude of the estimated hit rate per unit area is of the order of the kHz for the fully
 686 opened source. Moreover, taking profit of the two working absorbers, it will be possible to scan
 687 background rates at 0 Hz, ~ 300 Hz as well as ~ 600 Hz. Without source, a good estimate of the
 688 intrinsic performance will be available. Then at 300 Hz, the goal will be to show that the detectors
 689 fulfill the performance certification of CMS RPCs. Then a first idea of the performance of the
 690 detectors at higher background will be provided with absorption factors 2 (~ 600 Hz) and 1 (no
 691 absorption). *[Here I will also put a reference to the plot showing the estimated background rate at
 692 the level of RE3/1 in the case of HL-LHC but this one being in another chapter, I will do it later.]*

Nominal ABS	Photon flux F [$s^{-1}cm^{-2}$]			Hit rate/unit area [$Hz cm^{-2}$] at $D^{2014} = 206$ cm
	at $D_0^{1997} = 50$ cm	at $D_0^{1997} = 206$ cm	at $D^{2014} = 206$ cm	
1	$0.12 \cdot 10^8 \pm 0.2\%$	$0.84 \cdot 10^6 \pm 0.3\%$	$0.56 \cdot 10^6 \pm 0.3\%$	1129 ± 32
2	$0.68 \cdot 10^7 \pm 0.3\%$	$0.48 \cdot 10^6 \pm 0.3\%$	$0.32 \cdot 10^6 \pm 0.3\%$	640 ± 19
5	$0.31 \cdot 10^7 \pm 0.4\%$	$0.22 \cdot 10^6 \pm 0.3\%$	$0.15 \cdot 10^6 \pm 0.3\%$	292 ± 9

Table 5.3: The data at D_0 in 1997 is taken from [6]. In a second step, using Equations 5.8 and 5.9, the flux at D can be estimated in 1997. Then, taking into account the attenuation of the source activity, the flux at D can be estimated at the time of the tests in GIF in 2014. Finally, assuming a sensitivity of the RPC to γ $s = 2 \cdot 10^{-3}$, an estimation of the hit rate per unit area is obtained.

693 **5.2.4.2 Dose measurements**

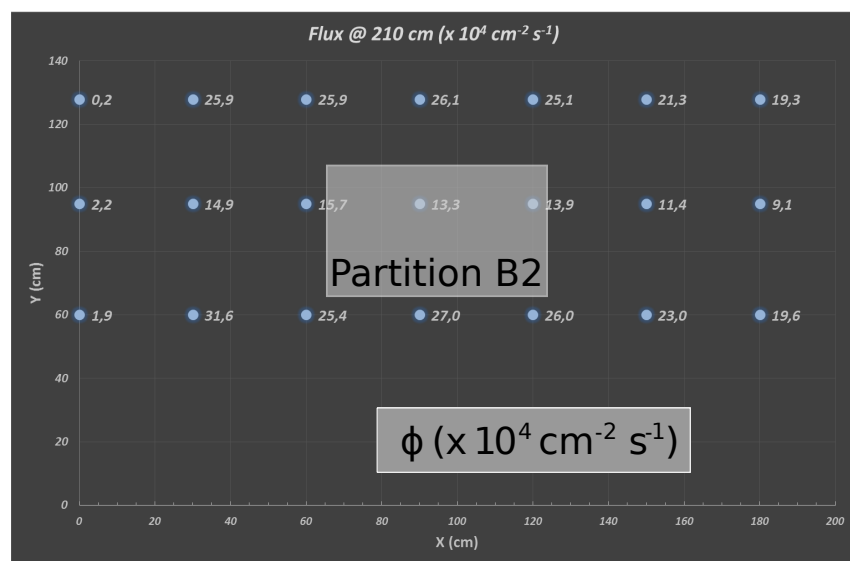


Figure 5.14: Dose measurements has been done in a plane corresponding to the tents front side. This plan is 1900 mm away from the source. As explained in the first chapter, a lens-shaped lead filter provides a uniform photon flux in the vertical plan orthogonal to the beam direction. If the second line of measured fluxes is not taken into account because of lower values due to experimental equipments in the way between the source and the tent, the uniformity of the flux is well showed by the results.

694 **5.2.5 Results and discussions**

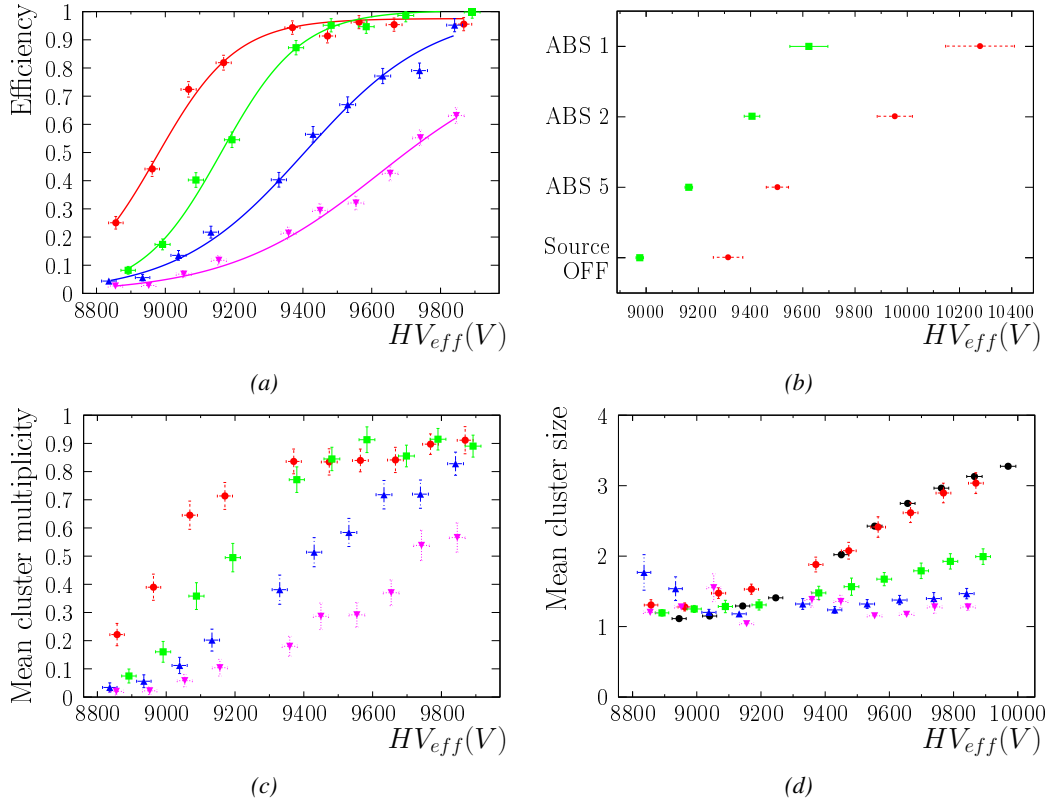


Figure 5.15

⁶⁹⁵ 5.3 Longevity tests at GIF++

⁶⁹⁶ Longevity studies imply a monitoring of the performance of the detectors probed using a high inten-
⁶⁹⁷ sity muon beam in a irradiated environment by periodically measuring their rate capability, the dark
⁶⁹⁸ current running through them and the bulk resistivity of the Bakelite composing their electrodes.
⁶⁹⁹ GIF++, with its very intense ^{137}Cs source, provides the perfect environment to perform such kind
⁷⁰⁰ of tests. Assuming a maximum acceleration factor of 3, it is expected to accumulate the equivalent
⁷⁰¹ charge in 1.7 years.

⁷⁰² As the maximum background is found in the endcap, the choice naturally was made to focus the
⁷⁰³ GIF++ longevity studies on endcap chambers. Most of the RPC system was installed in 2007. Nev-
⁷⁰⁴ ertheless, the large chambers in the fourth endcap (RE4/2 and RE4/3) have been installed during
⁷⁰⁵ LS1 in 2014. The Bakelite of these two different productions having different properties, four spare
⁷⁰⁶ chambers of the present system were selected, two RE2,3/2 spares and two RE4/2 spares. Having
⁷⁰⁷ two chambers of each type allows to always keep one of them non irradiated as reference, the per-
⁷⁰⁸ formance evolution of the irradiated chamber being then compared through time to the performance
⁷⁰⁹ of the non irradiated one.

⁷¹⁰ The performance of the detectors under different level of irradiation is measured periodically dur-
⁷¹¹ ing dedicated test beam periods using the H4 muon beam. In between these test beam periods, the
⁷¹² two RE2,3/2 and RE4/2 chambers selected for this study are irradiated by the ^{137}Cs source in order
⁷¹³ to accumulate charge and the gamma background is monitored, as well as the currents. The two
⁷¹⁴ remaining chambers are kept non-irradiated as reference detectors. Due to the limited gas flow in
⁷¹⁵ GIF++, the RE4 chamber remained non-irradiated until end of November 2016 where a new mass
⁷¹⁶ flow controller has been installed allowing for bigger volumes of gas to flow in the system.

⁷¹⁷ Figures 5.16 and 5.17 give us for different test beam periods, and thus for increasing integrated
⁷¹⁸ charge through time, a comparison of the maximum efficiency, obtained using a sigmoid-like func-
⁷¹⁹ tion, and of the working point of both irradiated and non irradiated chambers [8]. No aging is yet to
⁷²⁰ see from this data, the shifts in γ rate per unit area in between irradiated and non irradiated detec-
⁷²¹ tors and RE2 and RE4 types being easily explained by a difference of sensitivity due to the various
⁷²² Bakelite resistivities of the HPL electrodes used for the electrode production.

⁷²³ Collecting performance data at each test beam period allows us to extrapolate the maximum effi-
⁷²⁴ ciency for a background hit rate of $300\text{ Hz}/\text{cm}^2$ corresponding to the expected HL-LHC conditions.
⁷²⁵ Aging effects could emerge from a loss of efficiency with increasing integrated charge over time,
⁷²⁶ thus Figure 5.18 helps us understand such degradation of the performance of irradiated detectors in
⁷²⁷ comparison with non irradiated ones. The final answer for an eventual loss of efficiency is given in
⁷²⁸ Figure 5.19 by comparing for both irradiated and non irradiated detectors the efficiency sigmoids
⁷²⁹ before and after the longevity study. Moreover, to complete the performance information, the Bake-
⁷³⁰ lite resistivity is regularly measured thanks to Ag scans (Figure 5.20) and the noise rate is monitored
⁷³¹ weekly during irradiation periods (Figure 5.21). At the end of 2016, no signs of aging were observed
⁷³² and further investigation is needed to get closer to the final integrated charge requirements proposed
⁷³³ for the longevity study of the present CMS RPC sub-system.

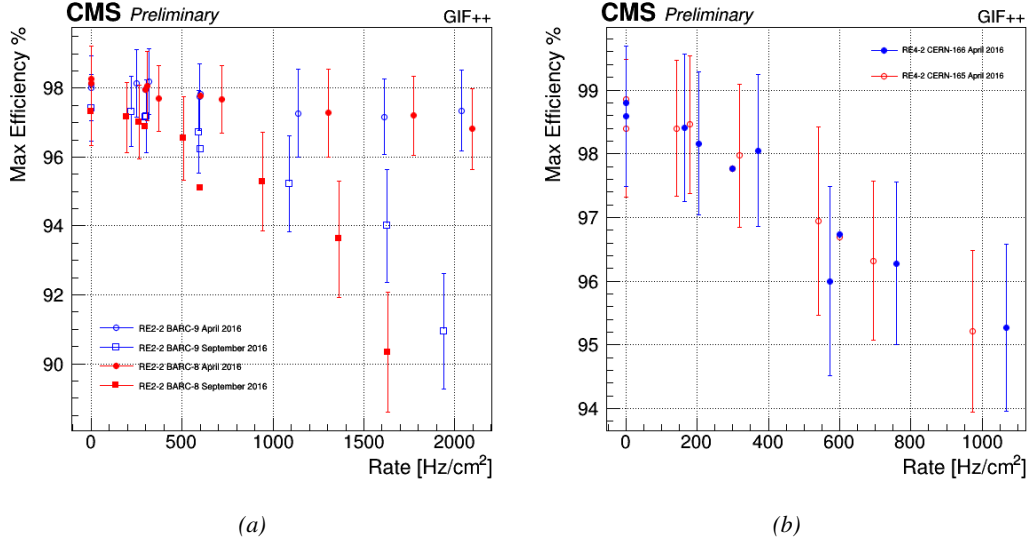


Figure 5.16: Evolution of the maximum efficiency for RE2 (5.16a) and RE4 (5.16b) chambers with increasing extrapolated γ rate per unit area at working point. Both irradiated (blue) and non irradiated (red) chambers are shown.

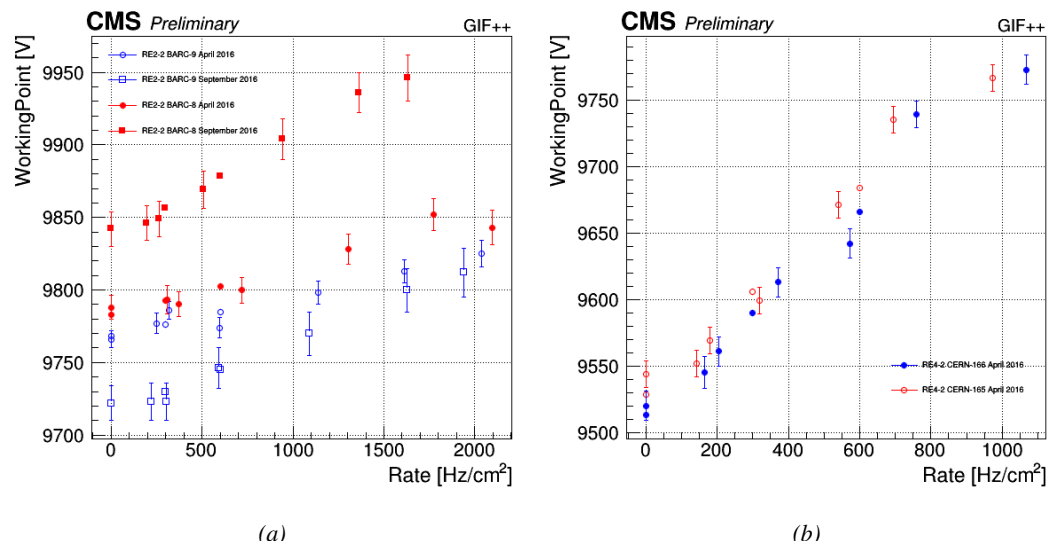


Figure 5.17: Evolution of the working point for RE2 (5.17a) and RE4 (5.17b) with increasing extrapolated γ rate per unit area at working point. Both irradiated (blue) and non irradiated (red) chambers are shown.

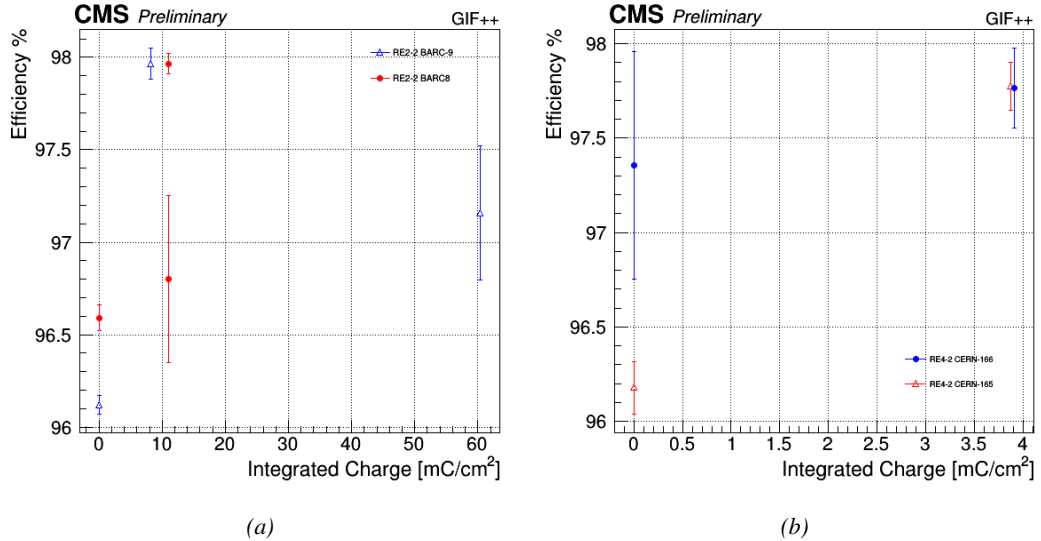


Figure 5.18: Evolution of the maximum efficiency at HL-LHC conditions, i.e. a background hit rate per unit area of $300 \text{ Hz}/\text{cm}^2$, with increasing integrated charge for RE2 (5.18a) and RE4 (5.18b) detectors. Both irradiated (blue) and non irradiated (red) chambers are shown. The integrated charge for non irradiated detectors is recorded during test beam periods and stays small with respect to the charge accumulated in irradiated chambers.

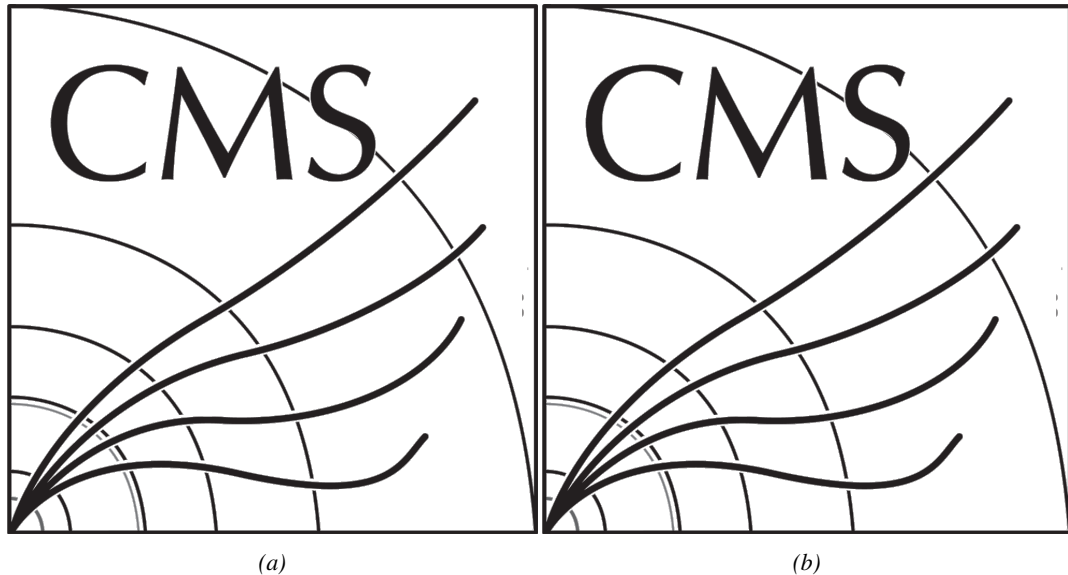


Figure 5.19: Comparison of the efficiency sigmoid before (triangles) and after (circles) irradiation for RE2 (5.19a) and RE4 (5.19b) detectors. Both irradiated (blue) and non irradiated (red) chambers are shown.

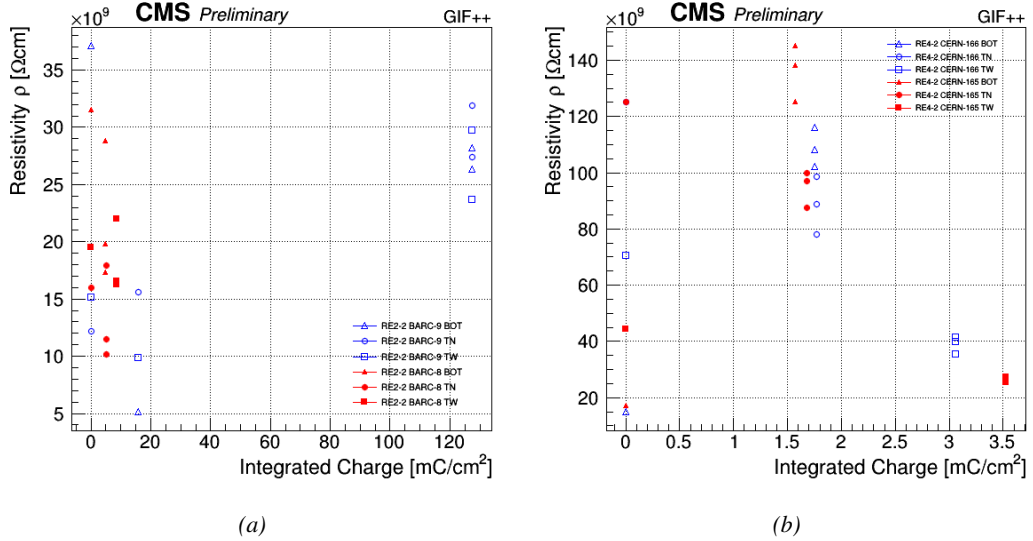


Figure 5.20: Evolution of the Bakelite resistivity for RE2 (5.20a) and RE4 (5.20b) detectors. Both irradiated (blue) and non-irradiated (red) chambers are shown.

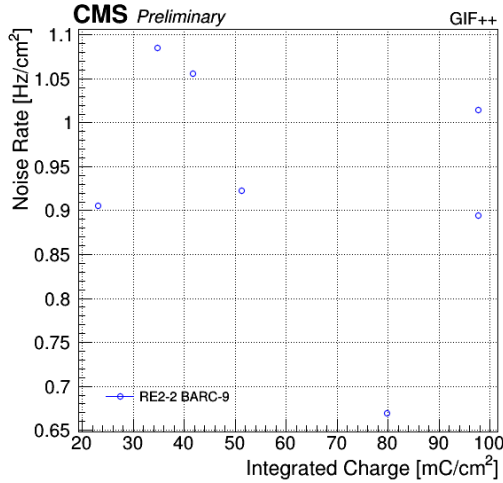


Figure 5.21: Evolution of the noise rate per unit area for the irradiated chamber RE2-2-BARC-9 only.

5.3.1 Description of the Data Acquisition

For the longevity studies, four spare chambers of the present system are used. Two spare RPCs of the RE2,3 stations as well as two spare RPCs from the new RE4 stations have been mounted in a Trolley. Six RE4 gaps are also placed in the trolley. The trolley is placed inside the GIFT++ in the upstream region of the bunker, taking the cesium source as a reference. The trolley is oriented for the detection surface of the chambers to be orthogonal to the beam line. The system can be moved along the orthogonal plane in order to have the beam in all η -partitions. For the aging the trolley is

742 moved outside the beam line and is placed in a distance of 5.2 m to the source, which irradiates the
 743 bunker using an attenuation filter of 2.2 which corresponds to a fluence of 10^7 gamma/cm^2 .

744 During GIF++ operation, the data collected can be divided into different categories as several
 745 parameters are monitored in addition to the usual RPC performance data. On one hand, to know
 746 the performance of a chamber, it is need to measure its efficiency and to know the background
 747 conditions in which it is operated. To do this, the hit signals from the chamber are recorded and
 748 stored in a ROOT file via a Data Acquisition (DAQ) software. On the other hand, it is also very
 749 important to monitor parameters such as environmental pressure and temperature, gas temperature
 750 and humidity, RPC HV, LV, and currents, or even source and beam status. This is done through the
 751 GIF++ web Detector Control Software (DCS) that stores this information in a database.

752 Two different types of tests are conducted on RPCs via the DAQ. Indeed, the performance of the
 753 detectors is measured periodically during dedicated test beam periods using the H4 muon beam. In
 754 between these test beam periods, when the beam is not available, the chambers are irradiated by the
 755 ^{137}Cs in order to accumulate deposited charge and the gamma background is measured.

756 RPCs under test are connected through LVDS cables to V1190A Time-to-Digital Converter
 757 (TDC) modules manufactured by CAEN. These modules, located in the rack area outside of the
 758 bunker, get the logic signals sent by the chambers and save them into their buffers. Due to the
 759 limited size of the buffers, the collected data is regularly erased and replaced. A trigger signal is
 760 needed for the TDC modules to send the useful data to the DAQ computer via a V1718 CAEN USB
 761 communication module.

762 In the case of performance test, the trigger signal used for data acquisition is generated by the
 763 coincidence of three scintillators. A first one is placed upstream outside of the bunker, a second one
 764 is placed downstream outside of the bunker, while a third one is placed in front of the trolley, close by
 765 the chambers. Every time a trigger is sent to the TDCs, i.e. every time a muon is detected, knowing
 766 the time delay in between the trigger and the RPC signals, signals located in the right time window
 767 are extracted from the buffers and saved for later analysis. Signals are taken in a time window of
 768 400 ns centered on the muon peak (here we could show a time spectrum). On the other hand, in the
 769 case of background rate measurement, the trigger signal needs to be "random" not to measure muons
 770 but to look at gamma background. A trigger pulse is continuously generated at a rate of 300 Hz using
 771 a dual timer. To integrate an as great as possible time, all signals contained within a time window of
 772 10us prior to the random trigger signal are extracted form the buffers and saved for further analysis
 773 (here another time spectrum to illustrate could be useful, maybe even place both spectrum together
 774 as a single Figure).

775 The signals sent to the TDCs correspond to hit collections in the RPCs. When a particle hits
 776 a RPC, it induce a signal in the pickup strips of the RPC readout. If this signal is higher than the
 777 detection threshold, a LVDS signal is sent to the TDCs. The data is then organised into 4 branches
 778 keeping track of the event number, the hit multiplicity for the whole setup, and the time and channel
 779 profile of the hits in the TDCs.

780 5.3.2 RPC current, environmental and operation parameter monitoring

781 In order to take into account the variation of pressure and temperature between different data taking
 782 periods the applied voltage is corrected following the relationship :

$$783 \quad HV_{eff} = HV_{app} \times \left(0.2 + 0.8 \cdot \frac{P_0}{P} \times \frac{T}{T_0} \right) \quad (5.10)$$

783 where T_0 (=293 K) and P_0 (=990 mbar) are the reference values.

784 **5.3.3 Measurement procedure**

785 Insert a short description of the online tools (DAQ, DCS, DQM).

786 Insert a short description of the offline tools : tracking and efficiency algorithm.

787 Identify long term aging effects we are monitoring the rates per strip.

788 **5.3.4 Longevity studies results**

6

789

790

Investigation on high rate RPCs

791 **6.1 Rate limitations and ageing of RPCs**

792 **6.1.1 Low resistivity electrodes**

793 **6.1.2 Low noise front-end electronics**

794 **6.2 Construction of prototypes**

795 **6.3 Results and discussions**

7

796

797

Conclusions and outlooks

798 **7.1 Conclusions**

799 **7.2 Outlooks**

References

- 801 [1] CERN. Geneva. LHC Experiments Committee. *The CMS muon project : Technical Design*
802 *Report*. Tech. rep. CERN-LHCC-97-032. CMS Collaboration, 1997.
- 803 [2] CERN. Geneva. LHC Experiments Committee. *Technical Proposal for the Phase-II Upgrade*
804 *of the CMS Detector*. Tech. rep. CERN-LHCC-2015-010. CMS Collaboration, 2015.
- 805 [3] CERN. Geneva. LHC Experiments Committee. *CMS, the Compact Muon Solenoid : technical*
806 *proposal*. Tech. rep. CERN-LHCC-94-38. CMS Collaboration, 1994.
- 807 [4] M. Abbrescia et al. “Study of long-term performance of CMS RPC under irradiation at the
808 CERN GIF”. In: *NIMA* 533 (2004), pp. 102–106.
- 809 [5] H.C. Kim et al. “Quantitative aging study with intense irradiation tests for the CMS forward
810 RPCs”. In: *NIMA* 602 (2009), pp. 771–774.
- 811 [6] S. Agosteo et al. “A facility for the test of large-area muon chambers at high rates”. In: *NIMA*
812 452 (2000), pp. 94–104.
- 813 [7] PoS, ed. *CERN GIF ++ : A new irradiation facility to test large-area particle detectors for*
814 *the high-luminosity LHC program*. Vol. TIPP2014. 2014, pp. 102–109.
- 815 [8] M. Abbrescia et al. “Cosmic ray tests of double-gap resistive plate chambers for the CMS
816 experiment”. In: *NIMA* 550 (2005), pp. 116–126.
- 817 [9] A. Fagot. *GIF++ DAQ v4.0*. 2017. URL: https://github.com/afagot/GIF_DAQ.
- 818 [10] CAEN. *Mod. V1190-VX1190 A/B, 128/64 Ch Multihit TDC*. 14th ed. 2016.
- 819 [11] CAEN. *Mod. V1718 VME USB Bridge*. 9th ed. 2009.
- 820 [12] W-Ie-Ne-R. *VME 6021-23 VXI*. 5th ed. 2016.
- 821 [13] Wikipedia. *INI file*. 2017. URL: https://en.wikipedia.org/wiki/INI_file.
- 822 [14] S. Carrillo A. Fagot. *GIF++ Offline Analysis v6*. 2017. URL: https://github.com/afagot/GIF_OfflineAnalysis.

A

824

825

826

A data acquisition software for CAEN VME TDCs

827 Certifying detectors in the perspective of HL-LHC required to develop tools for the GIF++ expe-
828 riment. Among them was the C++ Data Acquisition (DAQ) software that allows to make the com-
829 munications in between a computer and TDC modules in order to retrieve the RPC data [9]. In this
830 appendix, details about this software, as of how the software was written, how it functions and how
831 it can be exported to another similar setup, will be given.

832 A.1 GIF++ DAQ file tree

833 GIF++ DAQ source code is fully available on github at [https://github.com/afagot/GIF_](https://github.com/afagot/GIF_DAQ)
834 DAQ. The software requires 3 non-optional dependencies:

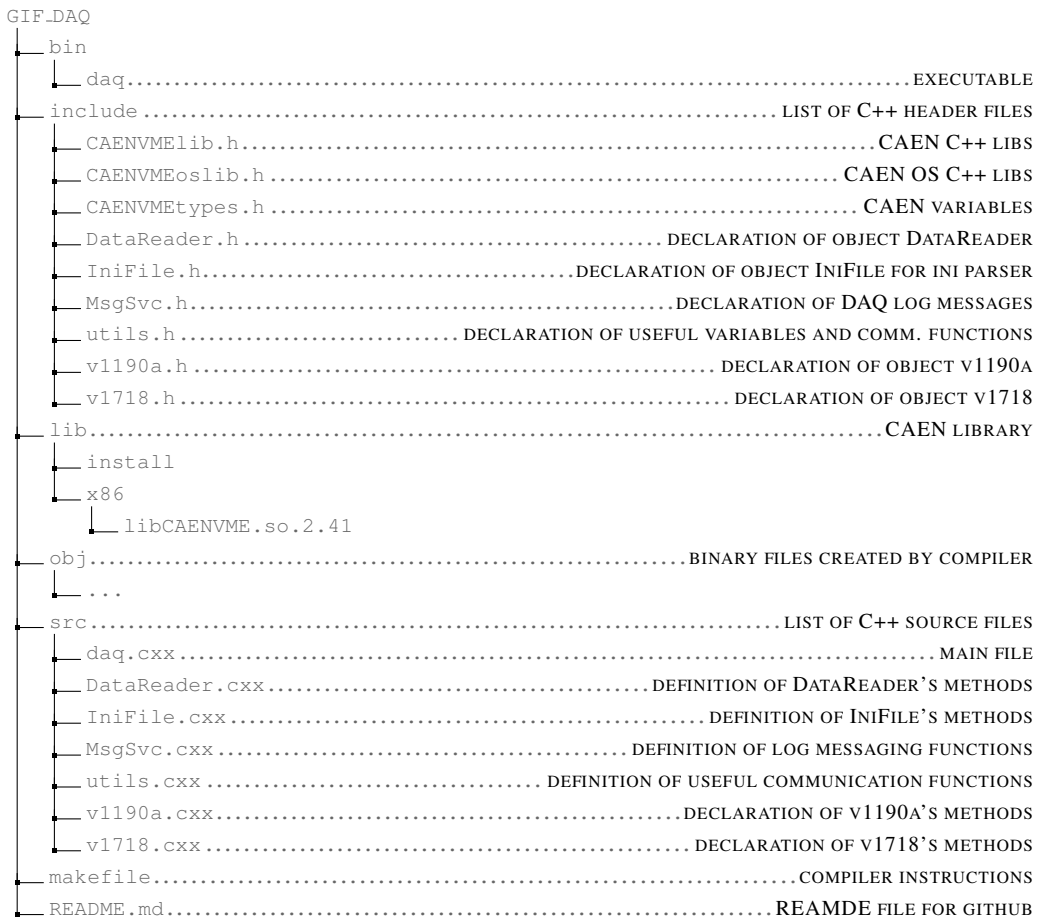
- 835 • CAEN USB Driver, to mount the VME hardware,
836 • CAEN VME Library, to communicate with the VME hardware, and
837 • ROOT, to organize the collected data into a TTree.

838 The CAEN VME library will not be packaged by distributions and will need to be installed
839 manually. To compile the GIF++ DAQ project via a terminal, from the DAQ folder use the command
840 :

841 make

842 The source code tree is provided below along with comments to give an overview of the files'
843 content. The different objects created for this project (`v1718`, `v1190a`, `IniFile` & `DataReader`) will
844 be described in details in the following sections.

845



846 A.2 Usage of the DAQ

847 GIF++ DAQ, as used in GIF++, is not a standalone software. Indeed, the system being more complexe,
 848 the DAQ only is a sub-layer of the software architecture developped to control and monitor
 849 the RPCs that are placed into the bunker for performance study in an irradiated environment. The top
 850 layer of GIF++ is a Web Detector Control System (webDCS) application. The DAQ is only called
 851 by the webDCS when data needs to be acquired. The webDCS operates the DAQ through command
 852 line. To start the DAQ, the webDCS calls:

853 bin/daq /path/to/the/log/file/in/the/output/data/folder
 854 where /path/to/the/log/file/in/the/output/data/folder is the only argument required.
 855 This log file is important for the webDCS as this file contains all the content of the communication
 856 of the webDCS and the different systems monitored by the webDCS. Its content is constantly
 857 displayed during data taking for the users to be able to follow the operations. The communication
 858 messages are normally sent to the webDCS log file via the functions declared in file MsgSvc.h,
 859 typically MSG_INFO(string message).

860

861 A.3 Description of the readout setup

862 The CMS RPC setup at GIF++ counts 5 V1190A Time-to-Digital Converter (TDC) manufactured
 863 by CAEN [10]. V1190A are VME units accepting 128 independent Multi-Hit/Multi-Event TDC
 864 channels whose signals are treated by 4 100 ps high performance TDC chips developed by CERN
 865 / ECP-MIC Division. The communication between the computer and the TDCs to transfer data is
 866 done via a V1718 VME master module also manufactured by CAEN and operated from a USB
 867 port [11]. These VME modules are all hosted into a 6U VME 6021 powered crate manufactured by
 868 W-Ie-Ne-R than can accommodate up to 21 VME bus cards [12]. These 3 components of the DAQ
 869 setup are shown in Figure A.1.

870

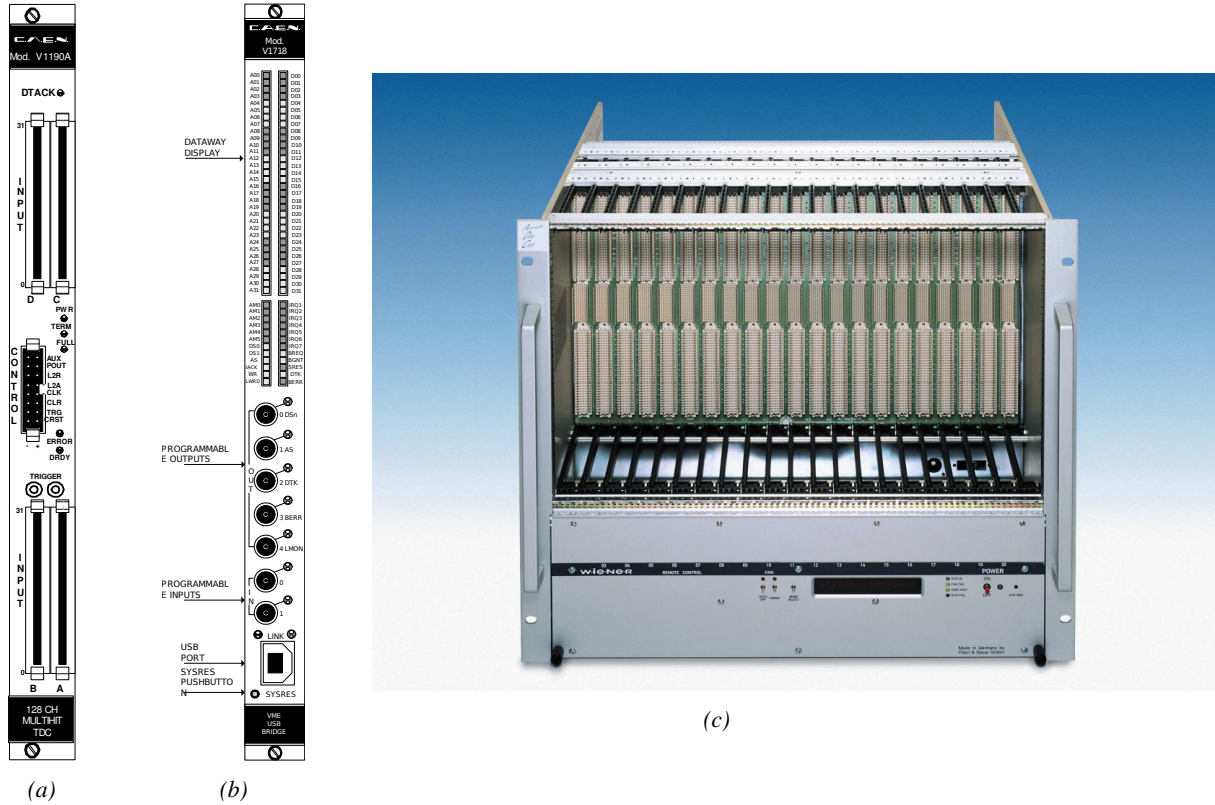


Figure A.1: (A.1a) View of the front panel of a V1190A TDC module [10]. (A.1b) View of the front panel of a V1718 Bridge module [11]. (A.1c) View of the front panel of a 6U 6021 VME crate [12].

871

A.4 Data read-out

872 To efficiently perform a data readout algorithm, C++ objects to handle the VME modules (TDCs
 873 and VME bridge) have been created along with objects to store data and read the configuration file
 874 that comes as an input of the DAQ software.

875

876 A.4.1 V1190A TDCs

877 The DAQ used at GIF takes profit of the *Trigger Matching Mode* offered by V1190A modules.
 878 This setting is enabled through the method `v1190a::SetTrigMatching (int ntdcs)` where `ntdcs`
 879 is the total number of TDCs in the setup this setting needs to be enabled for (Source Code A.1). A
 880 trigger matching is performed in between a trigger time tag, a trigger signal sent into the TRIGGER
 881 input of the TDC visible on Figure A.1a, and the channel time measurements, signals recorded from
 882 the detectors under test in our case. Control over this data acquisition mode, explained through
 883 Figure A.2, is offered via 4 programmable parameters:

- 884 • **match window:** the matching between a trigger and a hit is done within a programmable time
 885 window. This is set via the method
`void v1190a::SetTrigWindowWidth(Uint windowHeight, int ntdcs)`
- 887 • **window offset:** temporal distance between the trigger tag and the start of the trigger matching
 888 window. This is set via the method
`void v1190a::SetTrigWindowWidth(Uint windowHeight, int ntdcs)`
- 890 • **extra search margin:** an extended time window is used to ensure that all matching hits are
 891 found. This is set via the method
`void v1190a::SetTrigSearchMargin(Uint searchMargin, int ntdcs)`
- 893 • **reject margin:** older hits are automatically rejected to prevent buffer overflows and to speed
 894 up the search time. This is set via the method
`void v1190a::SetTrigRejectionMargin(Uint rejectMargin, int ntdcs)`

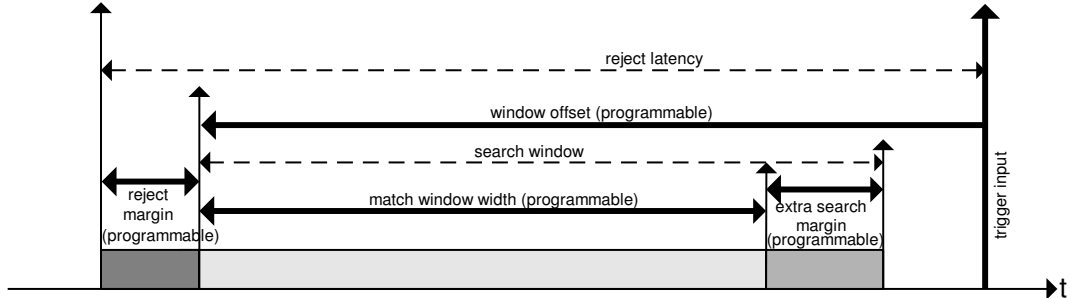


Figure A.2: Module V1190A Trigger Matching Mode timing diagram [10].

896 Each of these 4 parameters are given in number of clocks, 1 clock being 25 ns long. It is easy to
 897 understand at this level that there are 3 possible functioning settings:

- 898 • **1:** the match window is entirely contained after the trigger signal,
- 899 • **2:** the match window overlaps the trigger signal, or
- 900 • **3:** the match window is entirely contained before the trigger signal as displayed on Figure A.2.

901 In both the first and second cases, the sum of the window width and of the offset can be set to
 902 a maximum of 40 clocks, which corresponds to 1 μ s. Evidently, the offset can be negative, allowing
 903 for a longer match window, with the constraint of having the window ending at most 1 μ s after the
 904 trigger signal. In the third case, the maximum negative offset allowed is of 2048 clocks (12 bit) cor-
 905 responding to 51.2 μ s, the match window being strictly smaller than the offset. In the case of GIF++,

906 the choice has been made to use this last setting by delaying the trigger signal. During the studies
907 performed in GIF++, both the efficiency of the RPCs, probed using a muon beam, and the noise or
908 gamma background rate are monitored. The extra search and reject margins are left unused.
909 To probe the efficiency of RPC detectors, the trigger time tag is provided by the coïncidence of
910 scintillators when a bunch of muons passes through GIF++ area is used to trigger the data acquisi-
911 tion. For this measurement, it is useful to reduce the match window width only to contain the muon
912 information. Indeed, the delay in between a trigger signal and the detection of the corresponding
913 muon in the RPC being very contant (typically a few tens of ns due to jitter and cable length), the
914 muon signals are very localised in time. Thus, due to a delay of approximalety 325 ns in between
915 the muons and the trigger, the settings where chosen to have a window width of 24 clocks (600 ns)
916 centered on the muon peak thanks to a negative offset of 29 clocks (725 ns).
917 On the otherhand, monitoring the rates don't require for the DAQ to look at a specific time window.
918 It is important to integrate enough time to have a robust measurement of the rate as the number of
919 hits per time unit. The triggerring signal is provided by a pulse generator at a frequency of 300 Hz
920 to ensure that the data taking occurs in a random way, with respect to beam physics, to probe only
921 the irradiation spectrum on the detectors. The match window is set to 400 clocks (10 μ s) and the
922 negative offset to 401 clocks as it needs to exceed the value of the match window.

923

924 *Source Code A.1: Description of C++ object v1190a.*

```

class v1190a
{
private :
    long             Handle;
    vector<Data32>   Address;
    CVDataWidth      DataWidth;
    CVAddressModifier AddressModifier;

public:

v1190a(long handle, IniFile *inifile, int ntdcs);
~v1190a();
Data16 write_op_reg(Data32 address, int code, string error);
Data16 read_op_reg(Data32 address, string error);
void Reset(int ntdcs);
void Clear(int ntdcs);
void TestWR(Data16 value,int ntdcs);
void CheckTDCStatus(int ntdcs);
void CheckCommunication(int ntdcs);
void SetTDCTestMode(Data16 mode,int ntdcs);
void SetTrigMatching(int ntdcs);
void SetTrigTimeSubtraction(Data16 mode,int ntdcs);
void SetTrigWindowWidth(Uint windowHeight,int ntdcs);
void SetTrigWindowOffset(Uint windowOffset,int ntdcs);
void SetTrigSearchMargin(Uint searchMargin,int ntdcs);
void SetTrigRejectionMargin(Uint rejectMargin,int ntdcs);
void GetTrigConfiguration(int ntdcs);
void SetTrigConfiguration(IniFile *inifile,int ntdcs);
void SetTDCDetectionMode(Data16 mode,int ntdcs);
void SetTDCResolution(Data16 lsb,int ntdcs);
void SetTDCDeadTime(Data16 time,int ntdcs);
void SetTDCHeadTrailer(Data16 mode,int ntdcs);
void SetTDCEventSize(Data16 size,int ntdcs);
void SwitchChannels(IniFile *inifile,int ntdcs);
void SetIRQ(Data32 level, Data32 count,int ntdcs);
void SetBlockTransferMode(Data16 mode,int ntdcs);
void Set(IniFile *inifile,int ntdcs);
void CheckStatus(CVErrorCodes status) const;
int ReadBlockD32(Uint tdc, const Data16 address,
                 Data32 *data, const Uint words, bool ignore_berr);
Uint Read(RAWData *DataList,int ntdcs);
};

926 The v1190a object, defined in the DAQ software as in Source Code A.1, offers the possibility to
927 concatenate all TDCs in the readout setup into a single object containing a list of hardware addresses
928 (addresses to access the TDCs' buffer through the VME crate) and each constructor and method acts
929 on the list of TDCs.
930

```

931 A.4.2 DataReader

932 Enabled thanks to v1190a::SetBlockTransferMode(Data16 mode, int ntdcs), the data transfer
 933 is done via Block Transfer (BLT). Using BLT allows to tranfer a fixed number of events called a
 934 *block*. This is used together with an Almost Full Level (AFL) of the TDCs' output buffers, defined
 935 through v1190a::SetIRQ(Data32 level, Data32 count,int ntdcs). This AFL gives the maxi-
 936 mum amount of 32735 words (16 bits, corresponding to the depth of a TDC output buffer) that can
 937 writen in a buffer before an Interrupt Request (IRQ) is generated and seen by the VME Bridge,
 938 stopping the data acquisition to transfer the content of each TDC buffers before resuming. For each
 939 trigger, 6 words or more are written into the TDC buffer:

- 940 • a **global header** providing information of the event number since the beginning of the data
941 acquisition,
- 942 • a **TDC header**,
- 943 • the **TDC data** (*if any*), 1 for each hit recorded during the event, providing the channel and the
944 time stamp associated to the hit,
- 945 • a **TDC error** providing error flags,
- 946 • a **TDC trailer**,
- 947 • a **global trigger time tag** that provides the absolute trigger time relatively to the last reset,
948 and
- 949 • a **global trailer** providing the total word count in the event.

950 As previously described in Section 4.4.3, CMS RPC FEEs provide us with 100 ns long LVDS
951 output signals that are injected into the TDCs' input. Any avalanche signal that gives a signal above
952 the FEEs threshold is thus recorded by the TDCs as a hit within the match window. Each hit is
953 assigned to a specific TDC channel with a time stamp, with a precision of 100 ps. The reference
954 time, $t_0 = 0$, is provided by the beginning of the match window. Thus for each trigger, coming from
955 a scintillator coincidence or the pulse generator, a list of hits is stored into the TDCs' buffers and
956 will then be transferred into a ROOT Tree.

957

958 When the BLT is used, it is easy to understand that the maximum number of words that have
959 been set as AFL will not be a finite number of events or, at least, the number of events that would
960 be recorded into the TDC buffers will not be a multiple of the block size. In the last BLT cycle to
961 transfer data, the number of events to transfer will most probably be lower than the block size. In that
962 case, the TDC can add fillers at the end of the block but this option requires to send more data to the
963 computer and is thus a little slower. Another solution is to finish the transfer after the last event by
964 sending a bus error that states that the BLT reached the last event in the pile. This method has been
965 chosen in GIF++.

966

967 Due to irradiation, an event in GIF++ can count up to 300 words per TDC. A limit of 4096 words
968 (12 bits) has been set to generate IRQ which represent from 14 to almost 700 events depending on
969 the average of hits collected per event. Then the block size has been set to 100 events with enabled
970 bus errors. When an AFL is reached for one of the TDCs, the VME bridge stops the acquisition by
971 sending a BUSY signal.

972

973 The data is then transferred one TDC at a time into a structure called `RAWData` (Source Code A.2).

974

975 *Source Code A.2: Description of data holding C++ structure `RAWData`.*

```
struct RAWData {
    vector<int> *EventList;
    vector<int> *NHitsList;
    vector<int> *QFlagList;
    vector<vector<int> > *ChannelList;
    vector<vector<float> > *TimeStampList;
};
```

977 In order to organize the data transfer and the data storage, an object called `DataReader` was
978 created (Source Code A.3). On one hand, it has `v1718` and `v1190a` objects as private members for
979 communication purposes, such as VME modules settings via the configuration file `*iniFile` or data

980 read-out through `v1190a::Read()` and on the other hand, it contains the structure `RAWData` that allows
 981 to organise the data in vectors reproducing the tree structure of a ROOT file.

982

983 *Source Code A.3: Description of C++ object DataReader.*

```

class DataReader
{
    private:
        bool      StopFlag;
        IniFile *iniFile;
        Data32   MaxTriggers;
        v1718   *VME;
        int       nTDCs;
        v1190a  *TDCs;
        RAWData  TDCData;

    public:
        DataReader();
        virtual ~DataReader();
        void     SetIniFile(string inifilename);
        void     SetMaxTriggers();
        Data32   GetMaxTriggers();
        void     SetVME();
        void     SetTDC();
        int      GetQFlag(Uint it);
        void     Init(string inifilename);
        void     FlushBuffer();
        void     Update();
        string   GetFileName();
        void     WriteRunRegistry(string filename);
        void     Run();
};


```

985 Each event is transferred from `TDCData` and saved into branches of a ROOT `TTree` as 3 integers
 986 that represent the event ID (`EventCount`), the number of hits read from the TDCs (`nHits`), and the
 987 quality flag that provides information for any problem in the data transfer (`qflag`), and 2 lists of
 988 `nHits` elements containing the fired TDC channels (`TDCCh`) and their respective time stamps (`TDCTS`),
 989 as presented in Source Code A.4. The ROOT file file is named using information contained into
 990 the configuration file, presented in section A.5.2. The needed information is extracted using method
 991 `DataReader::GetFileName()` and allow to build the output filename format `ScanXXXXXX_HVX_DAQ.root`
 992 where `ScanXXXXXX` is a 6 digit number representing the scan number into GIF++ database and HVX
 993 the HV step within the scan that can be more than a single digit. An example of ROOT data file is
 994 provided with Figure A.3.

995

996 *Source Code A.4: Highlight of the data transfer and organisation within `DataReader::Run()` after the data
 has been collected into `TDCData`.*

```
RAWData TDCData;
TFile *outputFile = new TFile(outputFileName.c_str(),"recreate");
TTree *RAWDataTree = new TTree("RAWData","RAWData");

int EventCount = -9;
int nHits = -8;
int qflag = -7;
vector<int> TDCCh;
vector<float> TDCTS;

RAWDataTree->Branch("EventNumber",&EventCount, "EventNumber/I");
RAWDataTree->Branch("number_of_hits",&nHits,"number_of_hits/I");
RAWDataTree->Branch("Quality_flag",&qflag,"Quality_flag/I");
RAWDataTree->Branch("TDC_channel",&TDCCh);
RAWDataTree->Branch("TDC_TimeStamp",&TDCTS);

997
//...
//Here read the TDC data using v1190a::Read() and place it into
//TDCData for as long as you didn't collect the requested amount
//of data.
//...

for(Uint i=0; i<TDCData.EventList->size(); i++) {
    EventCount = TDCData.EventList->at(i);
    nHits = TDCData.NHitsList->at(i);
    qflag = TDCData.QFlagList->at(i);
    TDCCh = TDCData.ChannelList->at(i);
    TDCTS = TDCData.TimeStampList->at(i);
    RAWDataTree->Fill();
}
```

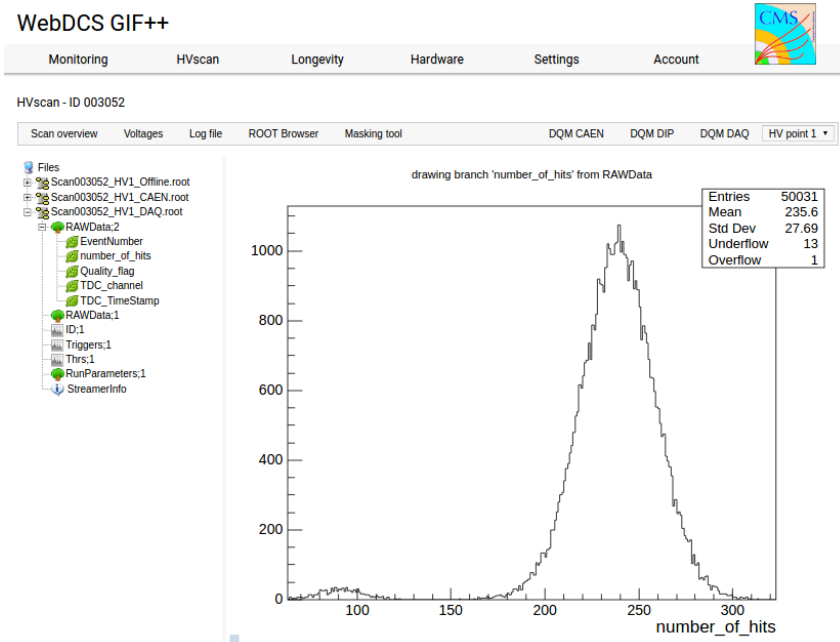


Figure A.3: Structure of the ROOT output file generated by the DAQ. The 5 branches (EventNumber, number_of_hits, Quality_flag, TDC_channel and TDC_TimeStamp) are visible on the left panel of the ROOT browser. On the right panel is visible the histogram corresponding to the variable nHits. In this specific example, there were approximately 50k events recorded to measure the gamma irradiation rate on the detectors. Each event is stored as a single entry in the TTree.

998 A.5 Communications

999 To ensure data readout and dialog in between the machine and the TDCs or in between the webDCS
1000 and the DAQ, different communication solutions were used. First of all, it is important to have a
1001 module to allow the communication in between the TDCs and the computer from which the DAQ
1002 operates. When this communication is effective, shifters using the webDCS to control data taking
1003 can thus send instructions to the DAQ.

1004

1005 A.5.1 V1718 USB Bridge

1006 In the previous section, the data transfer has been discussed. The importance of the `v1718` object
1007 (Source Code A.5), used as private member of `DataReader`, was not explicated. VME master
1008 modules are used for communication purposes as they host the USB port that connects the pow-
1009 ered crate buffer to the computer where the DAQ is installed. From the source code point of view,
1010 this object is used to control the communication status, by reading the returned error codes with
1011 `v1718::CheckStatus()`, or to check for IRQs coming from the TDCs through `v1718::CheckIRQ()`.
1012 Finally, to ensure that triggers are blocked at the hardware level, a NIM pulse is sent out of one of the
1013 5 programmable outputs (`v1718::SendBUSY()`) to the VETO of the coincidence module where the
1014 trigger signals originate from. As long as this signal is ON, no trigger can reach the TDCs anymore.

1015

1018 A.5.2 Configuration file

1019 The DAQ software takes as input a configuration file written using INI standard [13]. This file is
 1020 partly filled with the information provided by the shifters when starting data acquisition using the
 1021 webDCS, as shown by Figure A.4. This information is written in section `[General]` and will later
 1022 be stored in the ROOT file that contains the DAQ data as can be seen from Figure A.3. Indeed,
 1023 another `TTree` called `RunParameters` as well as the 2 histograms `ID`, containing the scan number,
 1024 start and stop time stamps, and `Triggers`, containing the number of triggers requested by the shifter,
 1025 are available in the data files. Moreover, `ScanID` and `HV` are then used to construct the file name
 1026 thanks to the method `DataReader::GetFileName()`.

WebDCS GIF++

Monitoring HVscan Longevity Hardware Settings Account



DAQ High Voltage Scan

Type scan:	Rate Scan	Comments:		
Source configuration:	Source OFF	U 333	D 333	
Beam configuration:	Beam OFF	HV after scan: Turn off		
Waiting time:	1	(min)		
Trigger mode:	<input type="checkbox"/> External	<input type="checkbox"/> Internal	<input type="checkbox"/> Random	
Minimal measure time:	10	(min)		

Chamber	RE2-2-NPD-BARC-8	RE2-2-CERN-105	RE2-2-NPD-BARC-9	RE4-2-CERN-105	RE4-2-KODEL-1-4	Max triggers
HV _{eff} 1	8600	8500	8600	8500	6500	
HV _{eff} 2	8700	8600	8700	8600	6600	
HV _{eff} 3	8800	8700	8800	8700	6700	
HV _{eff} 4	8900	8800	8900	8800	6800	
HV _{eff} 5	9000	8900	9000	8900	6900	
HV _{eff} 6	9100	9000	9100	9000	7000	
HV _{eff} 7	9200	9100	9200	9100	7100	
HV _{eff} 8	9300	9200	9300	9200	7200	
HV _{eff} 9	9400	9300	9400	9300	7300	
HV _{eff} 10	9500	9400	9500	9400	7400	

Start HV scan

Figure A.4: WebDCS DAQ scan page. On this page, shifters need to choose the type of scan (Rate, Efficiency or Noise Reference scan), the gamma source configuration at the moment of data taking, the beam configuration, and the trigger mode. These information will be stored in the DAQ ROOT output. Are also given the minimal measurement time and waiting time after ramping up of the detectors is over before starting the data acquisition. Then, the list of HV points to scan and the number of triggers for each run of the scan are given in the table underneath.

1027 The rest of the information is written beforehand in the configuration file template, as explicated
 1028 in Source Code A.6, and contains the hardware addresses to the different VME modules in the
 1029 setup as well as settings for the TDCs. As the TDC settings available in the configuration file are not
 1030 supposed to be modified, an improvement would be to remove them from the configuration file and
 1031 to hardcode them inside of the DAQ code itself or to place them into a different INI file that would
 1032 host only the TDC settings to lower the probability for a bad manipulation of the configuration file
 1033 that can be modified from one of webDCS' menus.

1034

1035 *Source Code A.6: INI configuration file template for 4 TDCs. In section [General], the number of TDCs is
 explicated and information about the ongoing run is given. Then, there are sections for each and every VME
 modules. There buffer addresses are given and for the TDCs, the list of channels to enable is given. Finally, in
 section [TDCSettings], a part of the TDC settings are given.*

```
[General]
TdcS=4
ScanID=$scanid
HV=$HV
RunType=$runtype
MaxTriggers=$maxtriggers
Beam=$beam
[VMEInterface]
Type=V1718
BaseAddress=0xFF0000
Name=VmeInterface
[TDC0]
Type=V1190A
BaseAddress=0x00000000
Name=Tdc0
StatusA00-15=1
StatusA16-31=1
StatusB00-15=1
StatusB16-31=1
StatusC00-15=1
StatusC16-31=1
StatusD00-15=1
StatusD16-31=1
[TDC1]
Type=V1190A
BaseAddress=0x11110000
Name=Tdc1
StatusA00-15=1
StatusA16-31=1
StatusB00-15=1
StatusB16-31=1
StatusC00-15=1
StatusC16-31=1
StatusD00-15=1
StatusD16-31=1
[TDC2]
Type=V1190A
BaseAddress=0x22220000
Name=Tdc2
StatusA00-15=1
StatusA16-31=1
StatusB00-15=1
StatusB16-31=1
StatusC00-15=1
StatusC16-31=1
StatusD00-15=1
StatusD16-31=1
[TDC3]
Type=V1190A
BaseAddress=0x44440000
Name=Tdc3
StatusA00-15=1
StatusA16-31=1
StatusB00-15=1
StatusB16-31=1
StatusC00-15=1
StatusC16-31=1
StatusD00-15=1
StatusD16-31=1
[TDCSettings]
TriggerExtraSearchMargin=0
TriggerRejectMargin=0
TriggerTimeSubtraction=0b1
TdcDetectionMode=0b01
TdcResolution=0b10
TdcDeadTime=0b00
TdcHeadTrailer=0b1
TdcEventSize=0b1001
TdcTestMode=0b0
BLTMode=1
```

1037 A.5.3 WebDCS/DAQ intercommunication

1038 When shifters send instructions to the DAQ via the configuration file, it is the webDCS itself that
 1039 gives the start command to the DAQ and then the 2 softwares use inter-process communication
 1040 through file to synchronise themselves. This communication file is represented by the variable `const`
 1041 `string __runstatuspath`.

1042 On one side, the webDCS sends commands or status that are readout by the DAQ:

- 1043 • INIT, status sent when launching a scan and read via function `CtrlRunStatus(...)`,
- 1044 • START, command to start data taking and read via function `CheckSTART()`,
- 1045 • STOP, command to stop data taking at the end of the scan and read via function `CheckSTOP()`,
 and
- 1047 • KILL, command to kill data taking sent by user and read via function `CheckKILL()`

1048 and on the other, the DAQ sends status that are controled by the webDCS:

- 1049 • DAQ_RDY, sent with `SendDAQReady()` to signify that the DAQ is ready to receive commands
 from the webDCS,
- 1051 • RUNNING, sent with `SendDAQRunning()` to signify that the DAQ is taking data,
- 1052 • DAQ_ERR, sent with `SendDAQError()` to signify that the DAQ didn't receive the expected
 command from the webDCS or that the launch command didn't have the right number of
 arguments,
- 1055 • RD_ERR, sent when the DAQ wasn't able to read the communication file, and
- 1056 • WR_ERR, sent when the DAQ wasn't able to write into the communication file.

1057 A.5.4 Example of inter-process communication cycle

1058 Under normal conditions, the webDCS and the DAQ processes exchange commands and status via
 1059 the file hosted at the address `__runstatuspath`, as explained in subsection A.5.3. An example of
 1060 cycle is given in Table A.1. In this example, the steps 3 to 5 are repeated as long as the webDCS tells
 1061 the DAQ to take data. A data taking cycle is the equivalent as what is called a *Scan* in GIFT++ jargon,
 1062 referring to a set a runs with several HV steps. Each repetition of steps 3 to 5 is then equivalent to a
 1063 single *Run*.

1064
 1065 At any moment during the data taking, for any reason, the shifter can decide that the data taking
 1066 needs to be stopped before it reached the end of the scheduled cycle. Thus at any moment on the
 1067 cycle, the content of the inter-process communication file will be changed to KILL and the DAQ
 1068 will shut down right away. The DAQ checks for KILL signals every 5s after the TDCs configu-
 1069 ration is over. So far, the function `CheckKILL()` has been used only inside of the data taking loop
 1070 of method `DataReader::Run()` and thus, if the shifter decides to KILL the data taking during the
 1071 TDC configuration phase or the HV ramping in between 2 HV steps, the DAQ will not be stopped
 1072 smoothly and a *force kill* command will be sent to stop the DAQ process that is still awake on the
 1073 computer. Improvements can be brought on this part of the software to make sure that the DAQ can
 1074 safely shutdown at any moment.

step	actions of webDCS	status of DAQ	__runstatuspath
1	launch DAQ ramp voltages ramping over wait for currents stabilization	readout of IniFile configuration of TDCs	INIT
2		configuration done send DAQ ready wait for START signal	DAQ_RDY
3	waiting time over send START		START
4	wait for run to end monitor DAQ run status	data taking ongoing check for KILL signal	RUNNING
5		run over send DAQ_RDY wait for next DCS signal	DAQ_RDY
6	ramp voltages ramping over wait for currents stabilization		DAQ_RDY
3	waiting time over send START		START
4	wait for run to end monitor DAQ run status	update IniFile information data taking ongoing check for KILL signal	RUNNING
5		run over send DAQ_RDY wait for next DCS signal	DAQ_RDY
7	send command STOP	DAQ shuts down	STOP

Table A.1: Inter-process communication cycles in between the webDCS and the DAQ through file string signals.

1076 **A.6 Software export**

1077 In section A.2 was discussed the fact that the DAQ as written in its last version is not a standalone
1078 software. It is possible to make it a standalone program that could be adapted to any VME setup
1079 using V1190A and V1718 modules by creating a GUI for the software or by printing the log mes-
1080 sages that are normally printed in the webDCS through the log file, directly into the terminal. This
1081 method was used by the DAQ up to version 3.0 moment where the webDCS was completed. Also, it
1082 is possible to check branches of DAQ v2.X to have example of communication through a terminal.
1083

1084 DAQ v2.X is nonetheless limited in it's possibilities and requires a lot of offline manual interven-
1085 tions from the users. Indeed, there is no communication of the software with the detectors' power
1086 supply system that would allow for a user a predefine a list of voltages to operate the detectors at
1087 and loop over to take data without any further manual intervention. In v2.X, the data is taken for a
1088 single detector setting and at the end of each run, the softwares asks the user if he intends on taking
1089 more runs. If so, the software invites the user to set the operating voltages accordingly to what is
1090 necessary and to manual update the configuration file in consequence. This working mode can be a
1091 very first approach before an evolution and has been successfully used by colleagues from different
1092 collaborations.

1093 For a more robust operation, it is recommended to develop a GUI or a web application to inter-
1094 face the DAQ. Moreover, to limit the amount of manual interventions, and thus the probability to
1095 make mistakes, it is also recommended to add an extra feature into the DAQ by installing the HV
1096 Wrapper library provided by CAEN of which an example of use in a similar DAQ software devel-
1097 opped by a master student of UGent, and called TinyDAQ, is provided on UGent's github. Then, this
1098 HV Wrapper will help you communicating with and give instructions to a CAEN HV powered crate
1099 and can be added into the DAQ at the same level where the communication with the user was made
1100 in DAQ v2.X. In case you are using another kind of power system for your detectors, it is stringly
1101 advised to use HV modules or crates that can be remotely controled via a using C++ libraries.
1102

1103

B

1104

1105

Details on the offline analysis package

1106 The data collected in GIF++ thanks to the DAQ described in Appendix A is difficult to interpret by a
1107 human user that doesn't have a clear idea of the raw data architecture of the CMS RPC ROOT files.
1108 In order to render the data human readable, a C++ offline analysis tool was designed to provide users
1109 with detector by detector histograms that give a clear overview of the parameters monitored during
1110 the data acquisition [14]. In this appendix, details about this software, as of how the software was
1111 written and how it functions will be given.

1112 B.1 GIF++ Offline Analysis file tree

1113 GIF++ Offline Analysis source code is fully available on github at https://github.com/afagot/GIF_OfflineAnalysis. The software requires ROOT as non-optionnal dependency
1114 as it takes ROOT files in input and write an output ROOT file containing histograms. To compile the
1115 GIF++ Offline Analysis project is compiled with cmake. To compile, first a build/ directory must
1116 be created to compile from there:

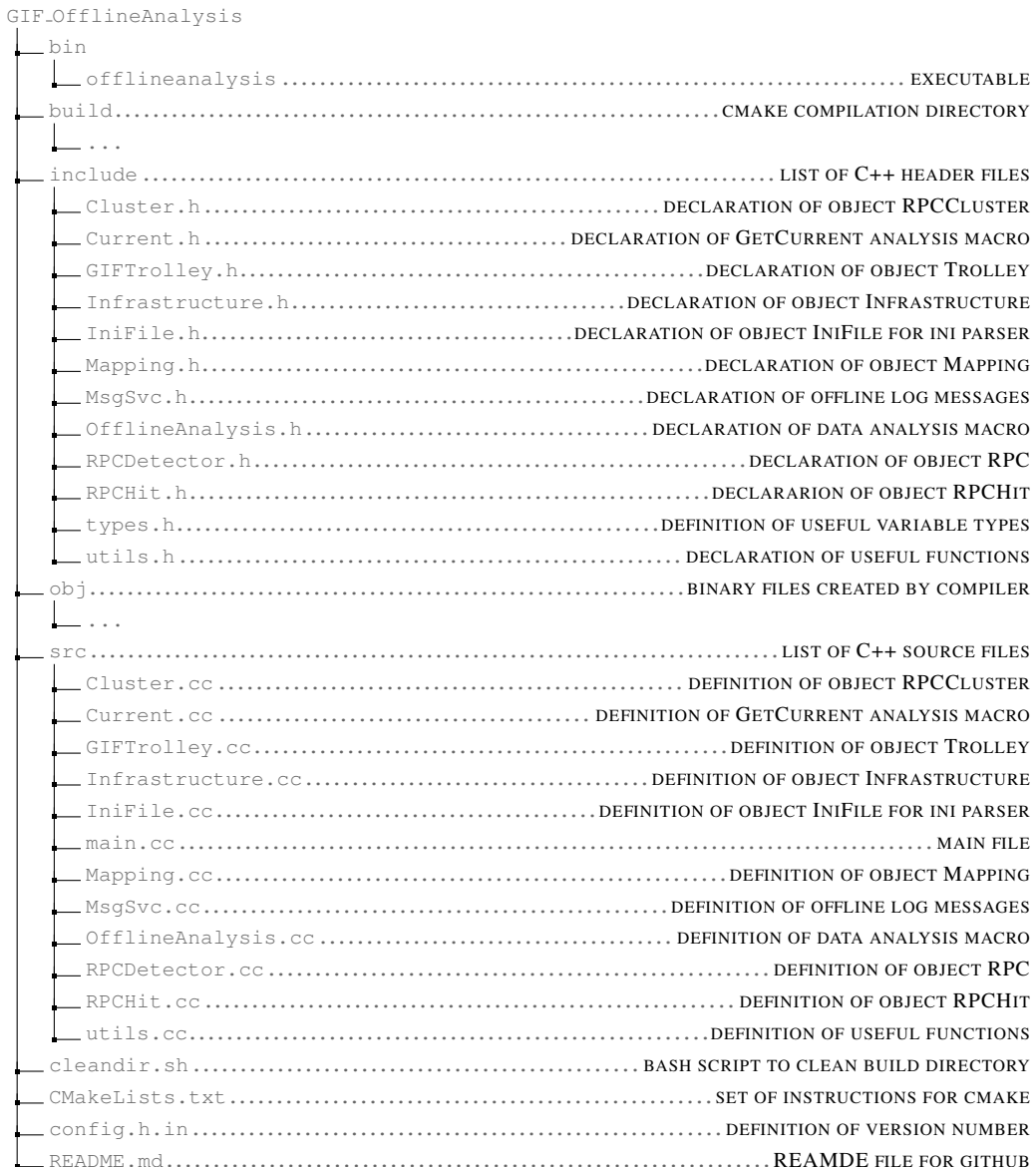
```
1117 mkdir build  
1118 cd build  
1119 cmake ..  
1120 make  
1121 make install
```

1119 To clean the directory and create a new build directory, the bash script cleandir.sh can be
1120 used:

```
1121 ./cleandir.sh
```

1122 The source code tree is provided below along with comments to give an overview of the files'
1123 content. The different objects created for this project (`Infrastructure`, `Trolley`, `RPC`, `Mapping`,
1124 `RPCHit`, `RPCCluster` and `Inifile`) will be described in details in the following sections.

1125



1126 B.2 Usage of the Offline Analysis

1127 In order to use the Offline Analysis tool, it is mandatory to know the Scan number and the HV Step
 1128 of the run that needs to be analysed. This information needs to be written in the following format:

1129 `Scan00XXXX_HVY`

1130 where XXXX is the scan ID and Y is the high voltage step (in case of a high voltage scan, data
 1131 will be taken for several HV steps). This format corresponds to the data file base name. Usually,
 1132 the offline analysis tool is automatically called by the WebDCS of GIF++ but, nonetheless, to locally
 1133 start the analysis for tests, simply type:

1134 `bin/offlineanalysis /path/to/Scan00XXXX_HVY`

1135 and the offline tool will by itself take care of finding the data ROOT files, as listed bellow:

- 1136 ● Scan00XXXX_HVY.DAQ.root containing the TDC data (events, hit and time lists)
- 1137 ● Scan00XXXX_HVY.CAEN.root containing the CAEN mainframe data (HVs and currents of
- 1138 every HV channels)

1139 The analysed output ROOT datafiles are saved into the data folder and called Scan00XXXX_HVY_Offline.root.
 1140 Inside those, a list of TH1 histograms can be found. Its size will vary as a function of the number of
 1141 detectors in the setup as each set of histograms is produced detector by detector. For each partition
 1142 of each chamber, you will find:

- 1143 ● Time_Profile_Tt_Sc_p shows the time profile of all recorded events,
- 1144 ● Hit_Profile_Tt_Sc_p shows the hit profile of all recorded events,
- 1145 ● Hit_Multiplicity_Tt_Sc_p shows the hit multiplicity of all recorded events (number of hits
 1146 per event),
- 1147 ● Strip_Mean_Noise_Tt_Sc_p shows noise/gamma rate for each strip in a selected time range,
- 1148 ● Strip_Activity_Tt_Sc_p shows noise/gamma activity for each strip (normalised version of
 1149 previous histogram - strip activity = strip rate / average partition rate),
- 1150 ● Strip_Homogeneity_Tt_Sc_p shows the homogeneity h of a given partition ($h = e^{-StdDev(strip rates in partition)}/(average$
- 1151 ● mask_Strip_Mean_Noise_Tt_Sc_p shows noise/gamma rate for each masked strip in a se-
 1152 lected time range,
- 1153 ● mask_Strip_Activity_Tt_Sc_p shows noise/gamma activity for each masked strip with repect
 1154 to the average rate of active strips,
- 1155 ● NoiseCSize_H_Tt_Sc_p shows noise/gamma cluster size,
- 1156 ● NoiseCMult_H_Tt_Sc_p shows noise/gamma cluster multiplicity (number of reconstructed
 1157 clusters per event),
- 1158 ● Chip_Mean_Noise_Tt_Sc_p shows the same information than Strip_Mean_Noise_Tt_Scp us-
 1159 ing a different binning (1 chip corresponds to 8 strips),
- 1160 ● Chip_Activity_Tt_Sc_p shows the same information than Strip_Activity_Tt_Scp using a
 1161 different binning,
- 1162 ● Chip_Homogeneity_Tt_Sc_p shows the homogeneity of a given partition using chip binning,
- 1163 ● Beam_Profile_Tt_Sc_p shows the estimated beam profile when taking efficiency scan (con-
 1164 structed with the hits contained in the muon peak where the noise/gamma background has
 1165 been subtracted),
- 1166 ● L0_Efficiency_Tt_Sc_p shows the level 0 efficiency that was estimated **without** muon track-
 1167 ing,
- 1168 ● MuonCSize_H_Tt_Sc_p shows the level 0 muon cluster size that was estimated **without** muon
 1169 tracking, and
- 1170 ● MuonCMult_H_Tt_Sc_p shows the level 0 muon cluster multiplicity that was estimated **without**
 1171 muon tracking.

1172 In the histogram labels, t stands for the trolley number (1 or 3), c for the chamber slot label in
1173 trolley t and p for the partition label (A, B, C or D depending on the chamber layout).

1174
1175 Moreover, up to 3 CSV files can be created depending on which ones of the 3 input files were in
1176 the data folder:

- 1177 • Offline-Rate.csv : contains the summary of the noise/gamma rates and clusters,
1178 • Offline-Current.csv : contains the summary of the currents and voltages applied on
1179 the RPCs,
1180 • Offline-L0-EffC1.csv : contains the summary of the level 0 efficiency and muon clus-
1181 ter information without tracking.

1182 Note that these 3 CSV files are created along their *headers* (file containing the names of the data
1183 columns) and are automatically merged together when the offline analysis is used via the RunDQM
1184 button of the webDCS. Thus, the resulting files are:

- 1185 • Rate.csv ,
1186 • Current.csv ,
1187 • L0-EffC1.csv .

C

1188

1189

Structure of the hybrid simulation software

1190 **C.1 Introduction**

1191 insert text here...

